

# Radio spectral properties at 150–5000 MHz of star-forming galaxies in the ELAIS-N1 field

Fangxia An,<sup>1,2\*</sup> M. Vaccari,<sup>2,3,4</sup> P. N. Best,<sup>5</sup> E. F. Ocran,<sup>6</sup> C. H. Ishwara-Chandra,<sup>7,3</sup> A. R. Taylor,<sup>3,2</sup> S. K. Leslie,<sup>8</sup> H. J. A. Röttgering,<sup>8</sup> R. Kondapally,<sup>5</sup> P. Haskell,<sup>9</sup> J. D. Collier,<sup>3,10</sup> M. Bonato<sup>4,11</sup>

<sup>1</sup>Purple Mountain Observatory, Chinese Academy of Sciences, 10 Yuanhua Road, Qixia District, Nanjing 210023, People's Republic of China

<sup>2</sup>Inter-University Institute for Data Intensive Astronomy, and Department of Physics and Astronomy, University of the Western Cape, Robert Sobukwe Road, 7535 Bellville, Cape Town, South Africa

<sup>3</sup>Inter-University Institute for Data Intensive Astronomy, and Department of Astronomy, University of Cape Town, Private Bag X3, Rondebosch 7701, South Africa

<sup>4</sup>INAF-Istituto di Radioastronomia, via Gobetti 101, 40129 Bologna, Italy

<sup>5</sup>Institute for Astronomy, University of Edinburgh, Royal Observatory, Blackford Hill, Edinburgh, EH9 3HJ, UK

<sup>6</sup>Korea Astronomy and Space Science Institute, 776 Daedeokdae-ro, Daejeon 305-348, Korea

<sup>7</sup>National Centre for Radio Astrophysics, Tata Institute of Fundamental Research, Pune 411007, India

<sup>8</sup>Leiden Observatory, Leiden University, PO Box 9513, NL- 2300 RA Leiden, The Netherlands

<sup>9</sup>Centre for Astrophysics Research, University of Hertfordshire, Hatfield, AL10 9AB, UK

<sup>10</sup>School of Science, Western Sydney University, Locked Bag 1797, Penrith, NSW 2751, Australia

<sup>11</sup>Italian ALMA Regional Centre, Via Gobetti 101, 40129 Bologna, Italy

Accepted XXX. Received YYY; in original form ZZZ

## ABSTRACT

By combining high-sensitivity LOFAR 150 MHz, uGMRT 400 MHz, GMRT 610 MHz, and JVLA 5 GHz data in the ELAIS-N1 field, we study the radio spectral properties of radio-detected star-forming galaxies (SFGs) at observer-frame frequencies of 150–5000 MHz. We select ~3,500 SFGs that have both LOFAR 150 MHz and GMRT 610 MHz detections by removing AGN from the two radio samples, and obtain a median spectral index of  $\alpha_{150}^{610} = -0.51 \pm 0.01$  with a scatter of  $\sigma = 0.2$ . Due to the relatively lower sensitivity of uGMRT 400 MHz data, we apply a flux cut of  $S_{610} > 300 \mu\text{Jy}$  and obtain the median spectral indices of  $\alpha_{150}^{385} = -0.42^{+0.03}_{-0.02}$ ,  $\alpha_{385}^{610} = -0.44^{+0.03}_{-0.04}$ , and  $\alpha_{150}^{610} = -0.42^{+0.02}_{-0.01}$  for the sample of 258 SFGs that have detections at these three radio frequencies. The JVLA 5 GHz observations only cover the central  $0.1 \text{ deg}^2$ , where ~100 SFGs are selected, for which we obtain median  $\alpha_{610}^{5000} = -1.14^{+0.04}_{-0.05}$ ,  $\alpha_{385}^{5000} = -1.08^{+0.01}_{-0.02}$  and  $\alpha_{150}^{5000} = -0.87 \pm 0.01$ , with some selection bias towards the steeper spectrum because of the high sensitivity of the 5 GHz data. Overall, the results show that the radio spectrum is flatter if we include a lower frequency dataset when measuring the radio spectral index at 150–5000 MHz. We study the correlations between radio spectral index and physical properties of radio-selected SFGs and find that, on average, the radio spectrum slightly steepens with increasing stellar mass. However, we only find that the radio spectrum flattens with increasing optical depth at V-band at  $\nu < \sim 1 \text{ GHz}$ . We suggest that spectral ageing due to the energy loss of cosmic ray electrons and thermal free-free absorption could be among the most likely physical mechanisms that drive the two correlations respectively. Both of these could be the physical causes of why the radio spectrum is flatter at low frequency than at high frequency.

**Key words:** radio continuum: galaxies – methods: observational – galaxies: formation –galaxy: evolution –galaxies: star formation –galaxies: statistics

## 1 INTRODUCTION

The radio continuum emission from star-forming galaxies (SFGs) consists of the non-thermal synchrotron radiation and thermal free-free emission. In SFGs, massive stars ( $M > 8 M_{\odot}$ ) explode to form Type II and Type Ib supernovae and accelerate cosmic ray (CR) electrons, which gyrate within large-scale galactic magnetic fields and produce radio emission via a synchrotron process (Voelk et al. 1989). The underlying physical process of free-free emission is pow-

ered by the Coulomb scattering between free ions and electrons in the HII regions, which are ionised by young, massive stars. Therefore, both of these processes are associated with massive star formation in galaxies. These characteristics, as well as the radio emission's insensitivity to dust attenuation, make the radio continuum a powerful tool to study the astrophysical properties of SFGs (see Condon 1992, for a review).

Although the free-free emission traces a nearly instantaneous star formation ( $< \sim 10 \text{ Myr}$ , Murphy et al. 2011, 2012; Kennicutt & Evans 2012), it is very challenging to target it at gigahertz frequencies or below due to its flat spectrum ( $\alpha \sim -0.1$ ,

\* E-mail: fangxiaan@pmo.ac.cn, fangxiaan@gmail.com

where  $S_\nu \propto \nu^\alpha$ ). At  $\nu > \sim 30$  GHz, thermal free-free radiation is expected to dominate the radio continuum emission, but the observation condition at such high-frequency range is stringent (Murphy et al. 2011, 2012; Algera et al. 2021, 2022). Therefore, although it is a delayed tracer of star formation ( $\sim 100$  Myr), the non-thermal synchrotron emission, which has a steep spectrum of  $\alpha \sim -0.8$ , is widely used to study activities of SFGs in both the local and distance Universe (e.g., Condon 1992; Bressan et al. 2002; Galvin et al. 2016; Pérez-Torres et al. 2021).

On galaxy-integrated scales, the radio continuum based star formation rate (SFR) is most often calibrated by an empirical correlation between far-infrared (FIR) and radio (typically at  $\sim 1.4$  GHz) luminosities (the FIRRC), which appears to hold across several orders of magnitude in spatial scale, luminosity, gas surface density and photon/magnetic field density and with a modest evolution with redshift (e.g., Helou et al. 1985; Yun et al. 2001; Bell 2003; Ivison et al. 2010; Mao et al. 2011; Magnelli et al. 2015; Hindson et al. 2018; Delvecchio et al. 2021). In addition, the FIRRC is also widely used to classify radio sources as either SFGs or radio-loud active galactic nuclei (AGN) because it is characteristic of radio-loud AGN activities to accelerate the CR electrons and cause an ‘excess’ of radio emission (e.g., Delvecchio et al. 2021; Whittam et al. 2022). Therefore, studies of SFGs based on radio continuum emission rely on a well-determined radio spectrum, especially at low frequency since the rest-frame  $\sim 1.4$  GHz is shifted to  $\nu < 1.4$  GHz at high redshift.

However, due to the lack (until recently) of high-sensitivity and large coverage low-frequency radio surveys and the fact that the radio spectra of SFGs are dominated by synchrotron radiation at  $\nu \sim 1 - 10$  GHz, most of the studies based on rest-frame radio spectra of SFGs assumed a synchrotron spectrum or a synchrotron spectrum with 10% contribution from the free-free emission ( $\alpha \sim -0.7$ ) when  $k$ -correcting the observed flux densities at  $\sim 1.4$  GHz (e.g., Magnelli et al. 2015; Hindson et al. 2018; Delvecchio et al. 2021). These assumptions will overestimate the radio flux density at low frequency because of a flattening of radio spectrum at  $\nu < \sim 1$  GHz as suggested by some recent works (Schleicher & Beck 2013; Delhaize et al. 2017; Galvin et al. 2018; Gim et al. 2019; An et al. 2021; Bonato et al. 2021).

At frequency  $\nu < \sim 1$  GHz, besides the two emission processes, the spectra of SFGs are expected to be affected by additional physical mechanisms. Notably, the HII regions become optically thick at  $\nu < \sim 1$  GHz, where free-free absorption causes greater attenuation of lower-frequency synchrotron radiation. This effect has been observed in the Galactic centre and some nearby galaxies (Wills et al. 1997; Roy 2013; Varenus et al. 2015), and it has been widely used to explain a flattening of radio spectrum at low frequency for both local and high-redshift galaxies (e.g., Condon 1992; McDonald et al. 2002; Murphy 2009; Clemens et al. 2010; Lacki 2013; Galvin et al. 2018; Klein et al. 2018; Dey et al. 2022). However, some other studies suggest that thermal gas absorption might not be the main cause of a flattening of radio spectrum at low frequency, since, for instance, there is no correlation between the inclination of the galaxies and the flatness of their radio spectrum at low frequency (Marvil et al. 2015; Chyży et al. 2018). Alternatively, the intrinsic steepening of the synchrotron spectrum, due to synchrotron and inverse Compton losses growing stronger at high CR energy, is used to explain why the high-frequency radio spectrum is steeper than the low-frequency in the literature (Marvil et al. 2015; Chyży et al. 2018; Thomson et al. 2019; An et al. 2021; Sweijen et al. 2022). Besides, the Razin-Tsytovich effect (Razin 1960), and the effects from relativistic bremsstrahlung and synchrotron self absorption are also expected to be more impor-

tant at low frequency (e.g., Fleishman & Tokarev 1995; Lacki 2010, 2013).

In recent years, the high-sensitivity and wide field extragalactic radio continuum surveys conducted by the Low Frequency Array (LOFAR, van Haarlem et al. 2013), Giant Metrewave Radio Telescope (GMRT, Swarup et al. 1991), and Murchison Widefield Array (MWA, Lonsdale et al. 2009) are finally allowing us to study the radio spectral properties at  $\nu_{\text{obs}} < \sim 1$  GHz with a statistically significant sample of SFGs.

In this work, we combine high-sensitivity LOFAR 150 MHz data, GMRT 610 MHz data, 400 MHz data from the upgraded GMRT (uGMRT), and 5 GHz data observed by the *Karl G. Jansky* Very Large Array (VLA) in the ELAIS-N1 field (European Large Area ISO Survey North 1, Oliver et al. 2000) to study radio spectral properties at observer-frame frequencies of 150–5000 MHz. Details of these radio data as well as the ancillary data used in this work are described in Section §2. We also summarise the main properties of these radio datasets in Table 1. We analyse the data and select SFGs from the radio surveys in Section §3. The measured radio spectral indices at different frequency ranges and the correlations between radio spectrum and physical properties of SFGs are presented in Section §4. Using these results, we discuss the underlying physical mechanisms that drive the radio spectrum at rest-frame  $\sim 150$ –10,000 MHz in Section §5. Our results are summarised in Section §6.

Throughout this paper, we adopt the AB magnitude system (Oke 1974) and assume a flat  $\Lambda$ CDM cosmological model with the Hubble constant  $H_0 = 67.27 \text{ km s}^{-1} \text{ Mpc}^{-1}$ , matter density parameter  $\Omega_m = 0.32$ , and cosmological constant  $\Omega_\Lambda = 0.68$  (Planck Collaboration et al. 2016).

## 2 OBSERVATIONS AND DATA

### 2.1 LOFAR 150 MHz data

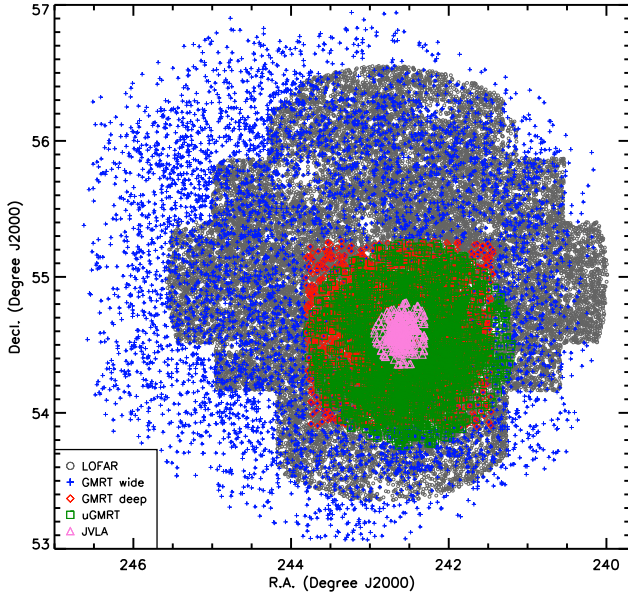
The LOFAR 150 MHz data of the ELAIS-N1 field used in this work are from the LOFAR Two Metre Sky Survey (LoTSS, Shimwell et al. 2017) Deep Fields (Tasse et al. 2021; Sabater et al. 2021). The observations were taken with the High Band Antenna (HBA) array with frequencies between 115–177 MHz in the LOFAR observation cycles 0, 2, and 4. The central frequency of the observation is 146.2 MHz. The final Stokes  $I$  image for all survey fields have a resolution of  $6''$ . The ELAIS-N1 field is the deepest of the LoTSS Deep Fields to date with an effective observing time of 163.7 hours (Sabater et al. 2021). The median RMS of the central  $6.7 \text{ deg}^2$ , where the highest-quality multi-wavelength data exists (from 0.15 to 500  $\mu\text{m}$ , Kondapally et al. 2021), is  $22.9 \mu\text{Jy beam}^{-1}$ . Within this region, Kondapally et al. (2021) created a final cross-matched and associated catalogue that contains 31,610 LOFAR 150 MHz radio sources (Figure 1). We refer the reader to Sabater et al. (2021) for more details about the observations and data reduction of LOFAR 150 MHz data and to Kondapally et al. (2021) for the creation of the final cross-matched and associated radio catalogue. We also present a short summary of the cross-matched results in Section §3.2.1.

### 2.2 uGMRT 400 MHz data

The ELAIS-N1 field was observed at 300–500 MHz with the uGMRT in GTAC cycle 32 (Chakraborty et al. 2019). The observations cover an area of  $\sim 1.8 \text{ deg}^2$ . With a total on-source time of  $\sim 13$  hours, the observations reach an RMS noise of  $\sim 15 \mu\text{Jy beam}^{-1}$  near the centre of the field. The angular resolution of the image is  $4''.6 \times 4''.3$ .

**Table 1.** Summary of the radio data sets used in this work

Data sets	Effective frequency MHz	bandwidth MHz	Coverage deg <sup>2</sup>	RMS noise <sup>a</sup> $\mu\text{Jy beam}^{-1}$	Angular resolution arcsecond (")	Number of sources
LOFAR 150 MHz	146.2	62	6.7	22.9	6	31,610
uGMRT 400 MHz	385	200	1.8	~15	4.6 × 4.3	2,528
GMRT 610 MHz (deep)	612	32	1.9	19.5	6	4,290
GMRT 610 MHz (wide)	612	32	12.8	~40	6	6,400
JVLA 5 GHz	5,000	2,000	0.1	1.1	2.5	387

<sup>a</sup> The median RMS noise for LOFAR 150 MHz, GMRT 610 MHz, and JVLA 5 GHz data and the off-source RMS noise near the centre of the field for uGMRT 400 MHz data.**Figure 1.** Distribution of radio sources detected by LOFAR, uGMRT, GMRT, and JVLA at 150 MHz, 400 MHz, 610 MHz, and 5 GHz respectively in the ELAIS-N1 field.

Chakraborty et al. (2019) detected 2,528  $> 6\sigma$  radio sources from the primary beam-corrected uGMRT 400 MHz image (Figure 1). Details of observation, data reduction, and source detection are presented in Chakraborty et al. (2019).

When analysing the data, Chakraborty et al. (2019) used the 400 MHz (the central frequency) as the effective frequency of their observations. However, there are some satellite radio-frequency interference (RFI) with about 20 MHz width near 480 MHz, which means the data is not divided equally below and above 400 MHz. We therefore estimate an effective frequency of 385 MHz by considering this effect. We test the reliability of this estimation by measuring the radio spectral indices at observer-frame frequencies of 150–385 MHz, 385–610 MHz and 150–610 MHz for GMRT 610 MHz-detected sources with  $S_{610\text{ MHz}} > 300 \mu\text{Jy}$ . As we present in Section §4.3.2, using 385 MHz as the effective frequency results in the median spectral indices that are consistent with those in the literature.

### 2.3 GMRT 610 MHz data

There are two sets of GMRT 610 MHz data of the ELAIS-N1 field used in this work. One is from the ELAIS-N1 610 MHz Deep Survey (GMRT deep, Ocran et al. 2020). The other is from a wide-area GMRT 610 MHz survey of the ELAIS-N1 field (GMRT wide,

Ishwara-Chandra et al. 2020). The GMRT deep data include a set of pointings from the GMRT wide survey (Ocran et al. 2020).

#### 2.3.1 GMRT deep

The ELAIS-N1 610 MHz Deep Survey covers an area of 1.86 deg<sup>2</sup> in the centre of the field. The survey was carried out with seven closely spaced GMRT pointings with a on-source integration time of ~18 hours for each pointing (Ocran et al. 2020). The seven pointings were mosaicked to create the final image. To reduce the noise around the edge, Ocran et al. (2020) also includes a set of pointings with on-source time of 2.5 hours per pointing from GMRT wide survey in the final mosaic image. The median RMS noise of the final mosaic image is 19.5  $\mu\text{Jy beam}^{-1}$  with a minimum noise of 7.1  $\mu\text{Jy beam}^{-1}$  in the central region. The angular resolution of the GMRT deep image is 6". Ocran et al. (2020) detected 4,290  $> 5\sigma$  radio sources from the final mosaic image (Figure 1). We refer the reader to Ocran et al. (2020) for more details.

#### 2.3.2 GMRT wide

The wide-area GMRT 610 MHz survey covers an area of 12.8 deg<sup>2</sup> in the ELAIS-N1 field by using a total of 51 GMRT pointings. The on-source time for each pointing is ~2.5 hours and for the final mosaic data is 153 hours. The final mosaic image reaches an RMS noise of ~40  $\mu\text{Jy beam}^{-1}$  and an angular resolution of 6". A total of 6,400 radio sources were detected from the final mosaic image (Figure 1). Details of observations, data reduction, and source extraction are presented in Ishwara-Chandra et al. (2020).

### 2.4 JVLA 5 GHz data

The JVLA 5 GHz observations only cover the central 0.13 deg<sup>2</sup> of the ELAIS-N1 field (Taylor et al. 2014). The bandwidth of the observation is 2 GHz and the central frequency is 5 GHz. With a total of 60 hours observation time, the JVLA 5 GHz data reaches an RMS noise of 1.05  $\mu\text{Jy beam}^{-1}$ . The angular resolution of the image is 2".5. In total, Taylor et al. (2014) detected 387 radio sources with  $S_{5\text{ GHz}} > 5 \mu\text{Jy}$  from the image. Although Taylor et al. (2014) only focus on the polarized emission from these sources, we include their continuum emission in this work to measure the radio spectral index between the observer-frame frequencies of 150–5000 MHz.

### 2.5 Additional Multi-wavelength Data/Catalogues

The ELAIS-N1 field was originally chosen for deep extra-galactic observations with the Infrared Space Observatory (ISO) due to its low infrared background (Rowan-Robinson et al. 2004; Vaccari et al. 2005). The deep infrared as well as the ultraviolet (UV) and optical observations make this field one of the best-studied astronomical



fields. Since this work is based on the radio-selected SFGs, we do not use these multi-wavelength data directly but utilize the cross-matched results of GMRT 610 MHz radio sources from [Ocran et al. \(2020\)](#) and of LOFAR 150 MHz sources from [Kondapally et al. \(2021\)](#). We therefore give a short summary of the multi-wavelength data used in the cross-matches in their works and refer the reader to [Ocran et al. \(2020\)](#) and [Kondapally et al. \(2021\)](#) for more details of these data.

[Ocran et al. \(2020\)](#) determined the multi-wavelength counterparts of GMRT 610 MHz-detected radio sources by using the Spitzer Extragalactic Representative Volume Survey (SERVS) DR2 firstly ([Mauduit et al. 2012](#); [Vaccari 2015](#)). The SERVS Data Fusion project included most of the publicly available far-UV to FIR data and homogenized these data to estimate the photometric and spectroscopic redshifts for IRAC 3.6  $\mu\text{m}$  and/or 4.5  $\mu\text{m}$ -selected sources ([Vaccari 2015](#)). Furthermore, if a SERVS match was not found, [Ocran et al. \(2020\)](#) used the *J* and *K*-band data from the UKIRT Infrared Deep Sky Survey (UKIDSS) Deep Extragalactic Survey (DXS) (DR10, [Lawrence et al. 2007](#)) to identify counterparts to GMRT 610 MHz radio sources. We will be back to their cross-matched results in Section §3.

In addition to the deep 3.6  $\mu\text{m}$  and 4.5  $\mu\text{m}$  from the SERVS and near-infrared (NIR) *J* and *K*-band data from UKIDSS-DIS, the following datasets were also used by [Kondapally et al. \(2021\)](#):

- (i) UV data from the Deep Imaging Survey (DIS) taken with the Galaxy Evolution Explorer (GALEX) space telescope ([Martin et al. 2005](#); [Morrissey et al. 2007](#)),
- (ii) *u*-band data from the Spitzer Adaptation of the Red-sequence Cluster Survey (SpARCS, [Wilson et al. 2009](#); [Muzzin et al. 2009](#)),
- (iii) optical *g*, *r*, *i*, *z*, and *y*-band data from the Medium Deep Survey (MDS), one of the Panoramic Survey Telescope and Rapid Response System (Pan-STARRS-1) surveys ([Chambers et al. 2016](#)),
- (iv) the *g*, *r*, *i*, *z*, *y*-band, and the narrowband NB921 data from the Hyper-Suprime-Cam Subaru Strategic Program (HSC-SSP) survey ([Aihara et al. 2018](#)), and
- (v) the mid-infrared (MIR) 3.6  $\mu\text{m}$ , 4.5  $\mu\text{m}$ , 5.8  $\mu\text{m}$ , and 8.0  $\mu\text{m}$  data from the Spitzer Wide-area Infra-Red Extragalactic (SWIRE) survey ([Lonsdale et al. 2003](#)).

In addition, [Kondapally et al. \(2021\)](#) included the far-infrared (FIR) data at 24  $\mu\text{m}$  from the Multi-band Imaging Photometer for Spitzer ([Rieke et al. 2004](#)) and at 100  $\mu\text{m}$ , 160  $\mu\text{m}$ , 250  $\mu\text{m}$ , 360  $\mu\text{m}$ , and 520  $\mu\text{m}$  from Herschel Multi-tiered Extragalactic survey (HerMES, [Oliver et al. 2012](#)) in their multi-wavelength photometric catalogue that were used to cross-match with the LOFAR 150 MHz radio sources. We will introduce their cross-matched results in Section §3.

### 3 ANALYSIS

To investigate the radio spectral properties of radio-detected sources, we first check the consistency of the astrometry of sources detected at different radio frequencies. Then, we introduce the selection of SFGs from GMRT 610 MHz-detected sources in [Ocran et al. \(2020\)](#) and from LOFAR 150 MHz-detected sources in Best et al. submitted.

#### 3.1 Astrometry

To test the relative astrometry of the radio sources detected at different frequencies, we first cross-match the radio sources detected at LOFAR 150 MHz, GMRT 610 MHz, uGMRT 400 MHz, and JVLA 5 GHz by using a matching radius of 10". As shown in the top panels

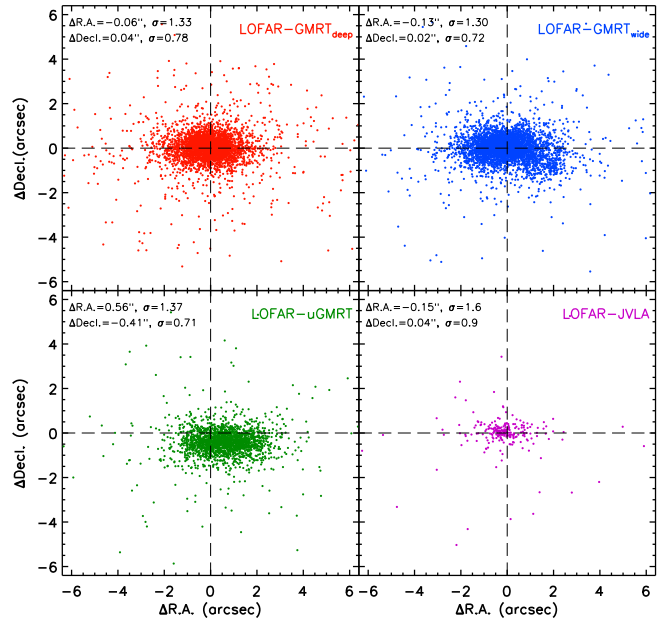


**Figure 2.** Comparisons between positions of sources detected in LOFAR 150 MHz, uGMRT 400 MHz, GMRT 610 MHz (both GMRT deep and GMRT wide), and JVLA 5 GHz images. Each pair of catalogues is matched by using a matching radius of 10". The astrometry of LOFAR 150 MHz sources is well-consistent with that of GMRT 610 MHz sources (both from deep and wide images) and JVLA 5 GHz as shown in the two top panels and bottom-right panel respectively. The astrometric offsets between uGMRT 400 MHz sources and sources detected from LOFAR 150 MHz are relatively larger as shown in the bottom-left panel.

of Figure 2, the astrometry of GMRT 610 MHz data, both GMRT deep and wide, is well-consistent with that of LOFAR 150 MHz data with the median offsets of  $\Delta R.A. \sim 0''.1$  and the  $\Delta Decl. \sim 0''.04$ . However, the median astrometric offsets between uGMRT 400 MHz and LOFAR 150 MHz data are  $\sim 0''.5$  in both right ascension and declination. Such offsets result in relatively larger cross-matching radii between 400 MHz sources and the sources detected at LOFAR 150 MHz and GMRT 610 MHz as described in Section §4.3. The bottom-right panel of Figure 2 shows that the astrometry of JVLA 5 GHz data is consistent with that of LOFAR 150 MHz data very well with the median offsets of  $\Delta R.A. = -0''.15$  and the  $\Delta Decl. = 0''.04$ .

#### 3.2 SFGs selection

Except the JVLA 5 GHz data, which have a very limited sky coverage, the LOFAR 150 MHz and GMRT 610 MHz (deep) data are the two deepest datasets that are utilised in studying radio spectral properties of the sources in this work. We therefore directly use the cross-matched results as well as the classification of SFGs and AGN in the two radio catalogues, i.e., the LOFAR 150 MHz catalogue presented in [Kondapally et al. \(2021\)](#) and the GMRT 610 MHz catalogue presented in [Ocran et al. \(2020\)](#).

##### 3.2.1 Cross-match and SFGs selection of 150 MHz sources

To produce a multi-wavelength photometric catalogue that is used for radio-optical/IR cross-match, [Kondapally et al. \(2021\)](#) first created the pixel-matched images by using 20 UV to mid-IR bands data in the ELAIS-N1 field. Sources were detected from a  $\chi^2$  sum of

optical SpARCS-*u*, PS1-*griz*, and NIR UKIDSS-DXS *J*, *K* imaging data and a separate  $\chi^2$  image that using only the Spitzer-IRAC 3.6  $\mu\text{m}$  and 4.5  $\mu\text{m}$  data from both the SWIRE and the SERVS (Section §2.5). This resulted in a multi-wavelength catalogue that contains  $\sim 1.5$  million sources in the overlapping region of Pan-STARRs, UKIDSS-DXS, and Spitzer-SWIRE surveys. These sources were used for cross-match with the LOFAR radio catalogue. For the 31,610 LOFAR 150 MHz sources within the overlapping region, 97.6% (30,839/31,610) of them have been identified with an optical, and/or NIR, and/or MIR counterpart in Kondapally et al. (2021).

The photometric redshift and optical depth of these 150 MHz sources were estimated from the best-fit spectral energy distributions (SEDs) by using the aperture-matched UV to MIR photometries presented in Kondapally et al. (2021). The photometric redshift was estimated by using a hybrid methodology that combines template fitting and machine learning. Details of the estimation are described in Duncan et al. (2021). For the sources with  $z < 1.5$ , Smith et al. (2021) estimated their physical properties, including the optical depth, by adopting the SED fitting code MAGPHYS (da Cunha et al. 2008). The fitting was done by determining the best-fit  $\chi^2$  between the photometry and all possible models that satisfy the energy balance criterion (which links the energy absorbed at short wavelengths with that re-radiated by dust in the FIR), assuming a two-component dust model from Charlot & Fall (2000) and an initial mass function from Chabrier (2003). The optical depth is the natural logarithm of the difference between the unattenuated and attenuated best-fit model spectrum at V-band.

To do the source classification for these 150 MHz sources, Best et al. (submitted) fitted the aperture-matched multi-wavelength photometries using four different SED fitting codes, two of which (CIGALE and AGNfitter; Noll et al. 2009; Calistro Rivera et al. 2016) included AGN templates in the fitting, and two of which (MAGPHYS and BAGPIPES; da Cunha et al. 2008; Carnall et al. 2018) did not. For CIGALE and AGNfitter, the output of the codes is the best estimate of the fraction of the mid-infrared light, which is contributed by the AGN ( $f_{\text{AGN}}$ ). Best et al. (submitted) used these two values of  $f_{\text{AGN}}$ , combined with information on whether the CIGALE and AGNfitter codes provided a better overall fit to the data than BAGPIPES and MAGPHYS, to determine whether there was evidence for the presence of a radiative AGN in the SED. A significant contribution to this classification is the behaviour of the SED through the mid-IR region of the spectrum, where previous mid-IR colour-colour selection techniques have been used to identify AGN (Donley et al. 2012). However, the use of the full SED information provides superior results, and is possible in ELAIS-N1 due to the high-quality multi-wavelength datasets. In total, Best et al. (submitted) classified 3,295 sources as hosting optical/IR AGN activity. For a total of 31,610 LOFAR 150 MHz sources, 1,072 of them are unable to be classified due to an absence of critical data, typically a photometric redshift.

In addition, Best et al. (submitted) also investigated the presence of radio AGN activity within the sample. Using the outputs of the four SED fitting codes, a consensus stellar mass and consensus SFR was derived for each object (see Best et al. (submitted) for details). Using an SFR to radio luminosity relation defined from the ridge-line of the distribution (which is broadly in line with the relation published by Smith et al. 2021), Best et al. (submitted) were able to identify those sources which showed more than 0.7 dex excess in radio luminosity relative to the value that would be predicted from their consensus SFR. In total, 4,797 sources were identified in this manner to be radio-excess AGN (of which 510 were also optical/IR selected AGN). And 1,314 sources remained unclassifiable.

Combining the two sets of classifications, we obtain a sample of 22,720 SFGs, after removing all objects which were either classified as AGN through optical/IR or radio-excess selection, or were unclassifiable due to a lack of relevant data in one of the two diagnostics.

For the radio-detected SFGs, except the photometric redshift and optical depth at V-band from Duncan et al. (2021) and Smith et al. (2021), we also use the consensus stellar mass from Best et al. submitted in Section §4.

### 3.2.2 Cross-match and SFGs selection of 610 MHz sources

For the 4,290 GMRT 610 MHz-detected sources in Ocran et al. (2020), 3,689 of them have a MIR counterpart from the SERVS and 3,542 have a NIR counterpart from the UKIDSS-DXS. Among them, 3,295 have been detected at both MIR and NIR. The multi-wavelength counterparts of these 610 MHz sources were identified by using their MIR and/or NIR positions. Based on these cross-match results, Ocran et al. (2020) carried out a multi-wavelength study using optical, X-ray, infrared, and radio diagnostics to identify AGN in their sample. We refer readers to Ocran et al. (2020) for more details of the cross-match and SFG/AGN classification. Here we briefly summarize the results of their classification.

For the 4,290 GMRT 610 MHz sources in Ocran et al. (2020), 3,490 of them have at least one measured multi-wavelength SFG/AGN classification diagnostic. Among them,

- 209 are classified as MIR AGN by adopting the MIR colour-colour selection criteria in Donley et al. (2012),
- 106 are optical spectroscopic AGN by using the BOSS CLASS and SUBCLASS parameters (Bolton et al. 2012),
- 102 are X-ray AGNs with  $L_X > 10^{42} \text{ erg s}^{-1}$ , and
- 340 are classified as radio loud AGN by comparing their MIR (MIPS 24  $\mu\text{m}$ ) to radio flux ratio (Bonzini et al. 2013).

We, therefore, remove a total of 648 AGNs and obtain a sample of 2,842 SFGs from the GMRT 610 MHz detected sources.

For the GMRT 610 MHz SFGs that have a LOFAR 150 MHz counterpart within  $2''.0$  (the cross-match radius of the two datasets as we discussed in Section §4.1), 70% of them were also classified as SFGs in Best et al. submitted. However, 25% of them were classified as AGN, specifically, 17% were classified as radio AGN in Best et al. submitted. Therefore, the different selections of radio AGN cause the major difference between the source classifications presented in Best et al. submitted and Ocran et al. (2020). The remaining 5% were unclassifiable due to a lack of measured diagnostic in Best et al. submitted. In this work, to obtain a clean sample of SFGs, we remove all AGN classified in Ocran et al. (2020) or Best et al. from our sample as presented in Section §4.

## 4 RESULTS

Because of the high sensitivity of LOFAR 150 MHz data, we use 610 MHz or 385 MHz as the selection frequency in studying radio spectral properties at observer-frame frequencies of 150–610 MHz and 150–385 MHz (Section §4.1 and §4.3) to obtain the relatively complete samples.

### 4.1 GMRT-DEEP 610 MHz as the selection frequency

We first use the GMRT-DEEP 610 MHz as the selection frequency to measure the radio spectral index at observer-frame frequencies of 150–610 MHz. To include all possible 150 MHz counterparts of

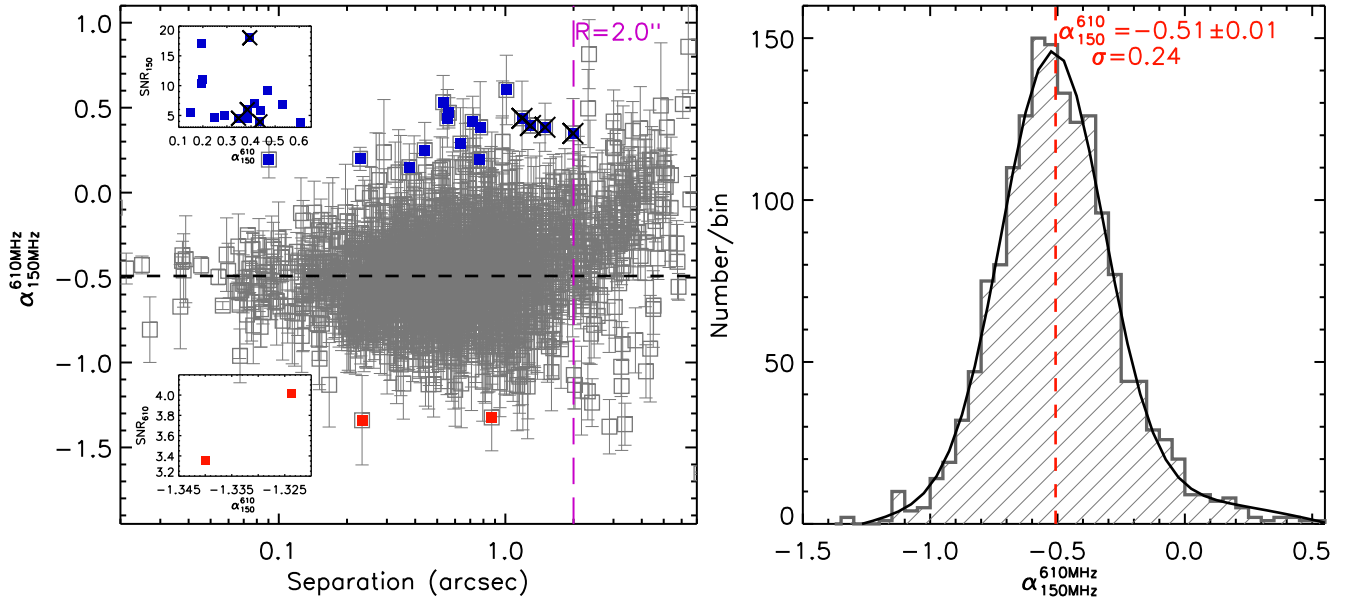


**Figure 3.** *Left:* Radio spectral index between the observer-frame frequencies of 150–610 MHz plotted against the separation between LOFAR 150 MHz and GMRT 610 MHz detections for the 1,782 SFGs. The blue squares are the 16 sources with  $r_{150-610} < 2''$  and  $\alpha_{150}^{610} - \sigma > 0.0$ . We show their SNR at 150 MHz as a function of  $\alpha_{150}^{610}$  in the top inset plot. We visually inspect both LOFAR 150 MHz and GMRT 610 MHz images and find that four of these 16 sources are resolved as two components at LOFAR 150 MHz, which are marked by black crosses. We, therefore, remove these four sources from our sample. There are also two sources with  $\alpha_{150}^{610} + \sigma < -1.0$ , which are marked by red squares. Visual inspection shows that both of them are faint at GMRT 610 MHz. *Right:* Distribution of radio spectral index,  $\alpha_{150}^{610}$ , of 1,590 SFGs with  $r_{150-610} < 2''$ . The median is  $\alpha_{150}^{610} = -0.51 \pm 0.01$  with a scatter of  $\sigma = 0.24$ .

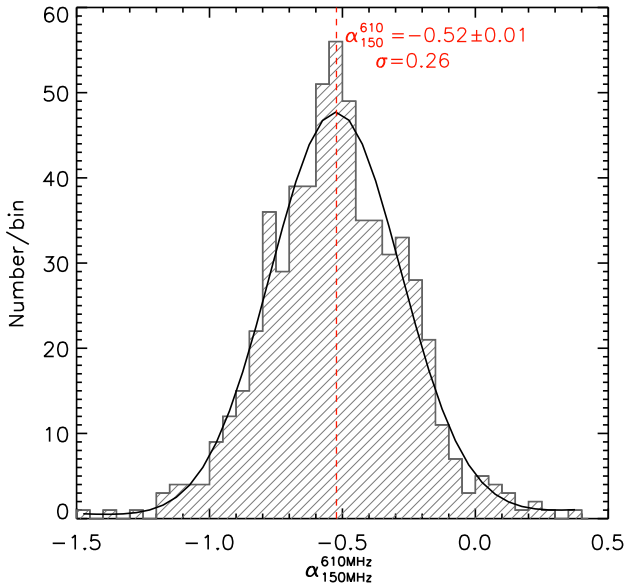


**Figure 4.** Distribution of radio spectral index at observed 150–610 MHz for the 596 GMRT 610 MHz-detected sources that lack measured SFG/AGN classification diagnostic in the GMRT-deep catalogue (Ocran et al. 2020). These sources have LOFAR 150 MHz counterparts within  $2''$  and are classified as SFGs in Best et al. submitted. The median is  $\alpha_{150}^{610} = -0.52 \pm 0.01$  (red dashed line) with a scatter of 0.26, which is consistent with the results from the sources classified as the SFGs in the GMRT-deep catalogue (Ocran et al. 2020), i.e., the results shown in Figure 3.

these 610 MHz-selected sources, we first use a cross-match radius of  $10''$ . For the 4,290 GMRT 610 MHz sources in Ocran et al. (2020), 87% (3,748/4,290) of them have a LOFAR 150 MHz counterpart

within  $10''$ . This fraction increases to 90% if we limit the 610 MHz sources to those with an associated redshift (Ocran et al. 2020). For the 2,842 GMRT 610 MHz-selected SFGs (Section §3.2.2), these fractions are also 87% (for all SFGs) and 90% (for SFGs with redshift) respectively.

#### 4.1.1 Radio spectral index between the observer-frame frequencies of 150–610 MHz

We first measure the radio spectral index at observer-frame frequencies of 150–610 MHz,  $\alpha_{150}^{610}$ , for a total of 2,462 GMRT 610 MHz-selected SFGs, which have a LOFAR 150 MHz counterpart within  $10''$ . The  $\alpha_{150}^{610}$  is measured by performing a linear fit in logarithmic space, and its uncertainty ( $\sigma_{150}^{610}$ ) is inherited from the uncertainties of the two flux densities. We show the  $\alpha_{150}^{610}$  as a function of the separation between the GMRT 610 MHz and LOFAR 150 MHz detections in Figure 3. The distribution of  $\alpha_{150}^{610}$  becomes asymmetric when the separation is greater than  $2''$  as shown in Figure 3. We therefore choose  $r_{150-610} = 2''$  as the cross-match radius when identifying the LOFAR 150 MHz counterparts for the 610 MHz selected SFGs. To reduce the contamination from AGN, we remove additional 590 GMRT 610 MHz sources that have a LOFAR 150 MHz counterpart within  $2''$  and are classified as AGN in Best et al. submitted. The left panel of Figure 3 shows the measured  $\alpha_{150}^{610}$  for the remaining 1,782 SFGs.

There are 16 SFGs with  $r_{150-610} < 2''$  but have the measured  $\alpha_{150}^{610} - \sigma_{150}^{610} > 0.0$  (very flat radio spectrum at 150–610 MHz). We show their SNR at 150 MHz as a function of  $\alpha_{150}^{610}$  in the top-left inset plot in Figure 3. We find that those SFGs with a flatter radio spectrum do have a lower SNR at 150 MHz. We also visually inspect both LOFAR 150 MHz and GMRT 610 MHz images and find that four of them are resolved as two components at LOFAR 150 MHz.



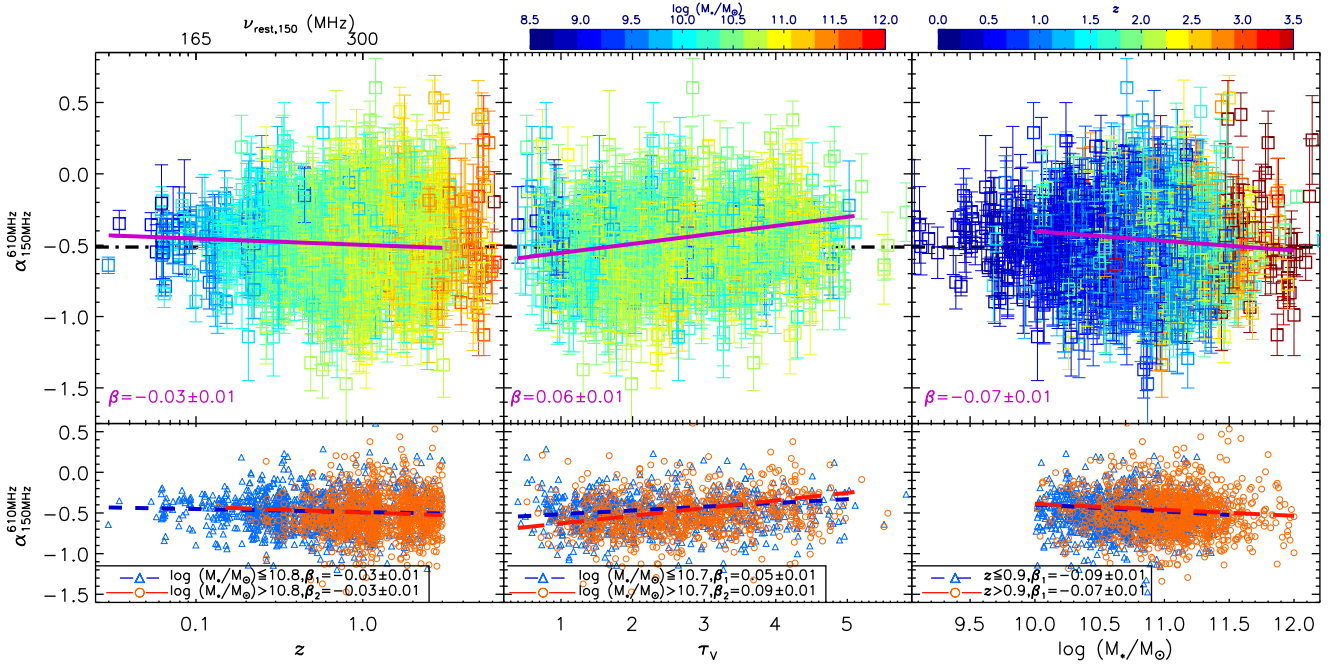


**Figure 5.** Radio spectral index between observer-frame frequencies of 150–610 MHz ( $\alpha_{150}^{610}$ ) as functions of redshift, rest-frame frequency corresponding to observed 150 MHz (left), optical depth at V-band (middle), and stellar mass (right) for the GMRT 610 MHz-selected SFGs. We have estimated photometric redshift and stellar mass for all of the 2,186 SFGs, and optical depth at V-band,  $\tau_V$ , for the 1,481 SFG with  $z < 1.5$ . The colour of symbols represents the stellar mass in the left-top and middle-top panels and represents redshift in the right-top panel as shown by the two color bars. On average, the radio spectral slope of SFGs at observed 150–610 MHz slightly flattens at low redshift (low frequency), flattens with increasing optical depth, and steepens with increasing stellar mass. To reduce the effect from the incompleteness of our radio flux-limited sample, we limit SFGs to  $z < 3$  and  $\log(M_*/M_\odot) > 10$  when fitting the correlations between  $\alpha_{150}^{610}$  and redshift, and stellar mass respectively. *Bottom:* We further divide our sample into the massive and the less-massive and find that the correlations between  $\alpha_{150}^{610}$  and redshift, optical depth at V-band of the two subsamples are independent from stellar mass. When studying the correlation between  $\alpha_{150}^{610}$  and stellar mass, we divide our sample into the high-redshift ( $z > 0.9$ , 1,049) and the low-redshift ( $z \leq 0.9$ , 1,015) subsamples and find that this correlation is independent from redshift.

We therefore remove them from our sample. There are also two sources with  $\alpha_{150}^{610} + \sigma_{\alpha_{150}^{610}} < -1.0$  (very steep radio spectrum at 150–610 MHz). Visual inspection shows that they are faint at GMRT 610 MHz.

There are 1,590 SFGs with  $r_{150-610} < 2''$  after we remove the four SFGs that are resolved at 150 MHz. We show the distribution of their  $\alpha_{150}^{610}$  in the right plot of Figure 3. The median is  $\alpha_{150}^{610} = -0.51 \pm 0.01$  with a scatter of  $\sigma = 0.24$  for these SFGs.

For the 4,290 GMRT 610 MHz-detected sources, 800 of them lack a measured diagnostic to classify them as SFGs or AGN in Ocran et al. (2020). Among them, 667 have a LOFAR 150 MHz counterparts within  $2''$  and 596/667 are classified as SFGs in Best et al. submitted. As shown in Figure 4, the median  $\alpha_{150}^{610}$  of these 596 SFGs is  $\alpha_{150}^{610} = -0.52 \pm 0.01$  with a standard deviation of  $\sigma = 0.26$ , which is highly consistent with the results shown in Figure 3. We therefore measure the radio spectral index at observer-frame frequencies of 150–610 MHz for 2,186 GMRT 610 MHz-selected SFGs in total.

For the GMRT 610 MHz-selected sources in Ocran et al. (2020), although the completeness of the detections at LOFAR 150 MHz is  $\sim 90\%$ , we further check these sources without LOFAR 150 MHz counterparts. There are 327 GMRT 610 MHz-selected sources with estimated photometric redshift in Ocran et al. (2020) but not included in the LOFAR final cross-matched catalogue (Kondapally et al. 2021). Our visual inspection shows that most of them are within the poor quality areas of the LOFAR map, such as near a bright source. We directly measure the pixel value at their 610 MHz posi-

tions and find 92% of them have the value  $> 100 \mu\text{Jy beam}^{-1}$ , which would correspond to a  $> 5\sigma$  detection in a cleaner part of the LOFAR image. Therefore, although these sources are not included in the LOFAR catalogue because of the inability to fit with a Gaussian profile, there is no reason to expect that this will bias our results.

#### 4.1.2 Radio spectral properties at 150–610 MHz

For the GMRT 610 MHz-selected SFGs, we show their radio spectral index between observer-frame frequencies of 150–610 MHz as functions of redshift, optical depth at V-band, and stellar mass in Figure 5. The photometric redshifts for the total 2,186 SFGs are from the LOFAR multi-wavelength photometric catalogue (Duncan et al. 2021). To reduce the effect from incompleteness of our radio flux-limited sample, we limit SFGs to  $z < 3$  when fitting the correlations between  $\alpha_{150}^{610}$  and redshift (rest-frame frequency). We perform a linear fit by minimizing the  $\chi^2$  and using the uncertainties of  $\alpha_{150}^{610}$  as the inverse weights. As shown in the left panel of Figure 5, on average, the radio spectral slope at observer-frame 150–610 MHz slightly flattens at low redshift (low frequency) with a  $\sim 3\sigma$  significance. We further divide our sample into the massive ( $\log(M_*/M_\odot) > 10.8$ ) and less-massive ( $\log(M_*/M_\odot) \leq 10.8$ ) subsamples with sample sizes of 1,040 and 1,020 respectively. The correlation between  $\alpha_{150}^{610}$  and redshift of the two subsamples are consistent with that of the full sample with a linear fit slope of  $\beta = -0.03 \pm 0.01$ , although the less-massive subsample is affected more by the incompleteness of our radio flux-limited sample.

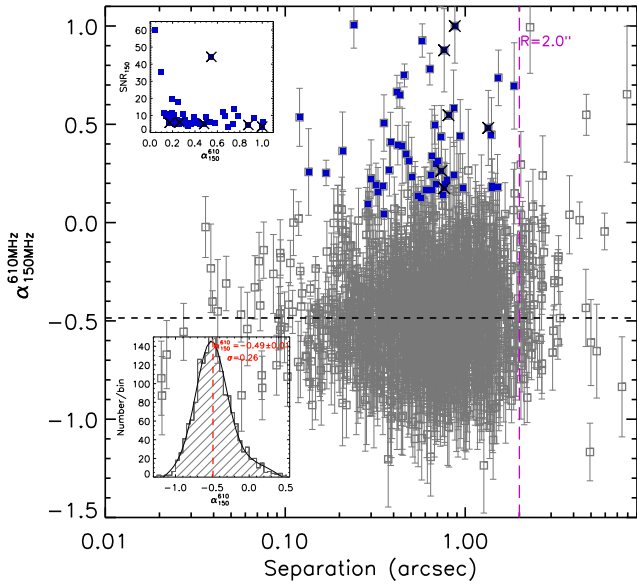


**Figure 6.** Radio spectral index between the observer-frame frequencies of 150–610 MHz plotted against the separation between LOFAR 150 MHz and GMRT 610 MHz detections for the 1,805 SFGs detected from GMRT-wide image data (Ishwara-Chandra et al. 2020). The purple dashed line marks the cross-match radius ( $r_{150-610} = 2''.0$ ) for identifying the LOFAR 150 MHz counterparts of the GMRT 610 MHz-detected sources. We mark the 48 sources with  $r_{150-610} < 2''.0$  and  $\alpha_{150}^{610} - \sigma > 0.0$  by blue squares. The top inset plot shows their SNR at 150 MHz as a function of  $\alpha_{150}^{610}$ . Our visual inspection shows that six of these 48 sources are resolved as two components at LOFAR 150 MHz, which are marked by black crosses. We remove these six sources from our sample and show the distribution of the radio spectral index for the remaining 1,711 SFGs with  $r_{150-610} < 2''.0$  in the bottom inset plot. The median radio spectral index between the observer-frame frequencies of 150–610 MHz for these 610 MHz-selected SFGs is  $\alpha_{150}^{610} = -0.49 \pm 0.01$  with a scatter of  $\sigma = 0.26$ .

In our sample, there are 1,481 SFGs with  $z < 1.5$ , which have estimated optical depth at V-band,  $\tau_V$ , from Smith et al. (2021). As shown in the middle panel of Figure 5, the radio spectrum at observer-frame 150–610 MHz flattens with increasing optical depth. The linear fit slope of this correlation is  $\beta = -0.06 \pm 0.01$ . We also divide the sample into massive ( $\log(M_*/M_\odot) > 10.7$ ) and less-massive ( $\log(M_*/M_\odot) \leq 10.7$ ) subsets with sample sizes of 718 and 763 respectively. We obtain the linear fit slopes of  $\beta = 0.09 \pm 0.01$  and  $\beta = 0.05 \pm 0.01$  for the two subsets respectively, which confirms that this trend is independent from the stellar mass of SFGs.

To reduce the effect of incompleteness, we limit our sample to  $\log(M_*/M_\odot) > 10$  when fitting the correlations between  $\alpha_{150}^{610}$  and stellar mass as shown in the right panel of Figure 5. On average, the radio spectral slope at observer-frame 150–610 MHz slightly steepens with increasing stellar mass for these radio-selected SFGs with a linear fit slope of  $\beta = -0.07 \pm 0.01$ . We further divide our sample into high-redshift ( $z > 0.9$ ) and low-redshift ( $z \leq 0.9$ ) subsets and find that this trend is independent from redshift, with the linear fit slopes being  $\beta = -0.07 \pm 0.01$  and  $\beta = -0.09 \pm 0.01$  respectively. These results are consistent with our previous work based on the MeerKAT and VLA data in the COSMOS field (An et al. 2021), although for a relatively higher frequency (observer-frame frequencies of 1.3–3 GHz).

## 4.2 GMRT-WIDE 610MHz as the selection frequency

We also use the relatively shallower but wide GMRT 610 MHz data from Ishwara-Chandra et al. (2020) to study radio spectral properties between observer-frame frequency of 150–610 MHz for radio-selected SFGs. For the 6,400 GMRT 610 MHz-detected sources (Ishwara-Chandra et al. 2020), 4,542 are within the region that has both LOFAR and multi-wavelength observations (Figure 1). Among them, 4,070 (90%) have a LOFAR 150 MHz counterparts within  $10''$  and 1,857 are classified as SFGs in Best et al. submitted. In addition, 1,258/6,400 overlap with GMRT-deep detected sources and 394 are classified as AGNs in Ocran et al. (2020). The overlap between the two AGN samples is 342. We therefore select a total of 1,805 SFGs and measure their spectral indices between observer-frame frequency of 150–610 MHz as shown in Figure 6.

We also adopt  $r_{150-610} = 2''.0$  as the cut when cross-matching the GMRT (wide) 610 MHz and LOFAR 150 MHz data as shown in Figure 6. There are 48 sources with  $r < 2''.0$  that have  $\alpha_{150}^{610} - \sigma_{150}^{610} > 0.0$  (very flat radio spectrum between observer-frame frequency of 150–610 MHz), and we show their SNR at 150 MHz as a function of  $\alpha_{150}^{610}$  in the top inset plot in Figure 6. We visually inspect both LOFAR 150 MHz and GMRT 610 MHz images and find that six of these 48 sources are resolved as two components at LOFAR 150 MHz. We therefore remove these six sources in the following analyses. Besides, as shown in the top inset plot of Figure 6, the sources with an extremely flatter radio spectrum at 150–610 MHz have lower SNR at 150 MHz. For the remaining 1,711 SFGs with  $r_{150-610} < 2''.0$ , we obtain a median radio spectral index of  $\alpha_{150}^{610} = -0.49 \pm 0.01$  with a scatter of  $\sigma = 0.26$ , which are well-consistent with the results based on the GMRT deep data (Section 4.1). We note that 396 of these SFGs are also included in the GMRT-deep sample shown in Figure 5.

For the 1,711 GMRT-wide-detected SFGs, 1,296 with  $z < 1.5$  have estimated optical depth at V-band,  $\tau_V$ , from Smith et al. (2021). As shown in Figure 7, on average, the radio spectrum at observed 150–610 MHz for the GMRT-wide-selected SFGs also slightly flattens with increasing optical depth and steepens with increasing stellar mass. However, we do not find the weak correlation between  $\alpha_{150}^{610}$  and redshift (rest-frame frequency). This might be caused by the sample of SFGs being not as clean as the one based on GMRT-deep-detected sources (Section 4.1). Overall, the radio spectral properties of GMRT-wide selected SFGs are consistent with those based on the GMRT-deep selected sample.

## 4.3 uGMRT 400 MHz as the selection frequency

We use the uGMRT 400 MHz-detected sources from Chakraborty et al. (2019) to study radio spectrum between observer-frame frequencies of 150–385 MHz and 385–610 MHz respectively. As we describe in Section 2.2, the effective frequency of uGMRT 400 MHz used in this work is 385 MHz. For the 2,528 uGMRT 400 MHz radio sources from Chakraborty et al. (2019), 2,219 (88%) have a LOFAR 150 MHz counterpart within  $10''$ . Among them, 1,255 are classified as SFGs in Best et al. submitted. In addition, 2,113 of the 2,528 uGMRT 400 MHz sources have a GMRT 610 MHz counterpart within  $10''$ . Among them, 1,180 are within  $2''.5$  and 401/1,180 are classified as AGNs in Ocran et al. (2020). The overlap between the two AGN samples from Best et al. submitted and Ocran et al. (2020) is 340. Therefore, we remove the additional 61 AGN from our sample and obtain a sample of 1,194 SFGs.



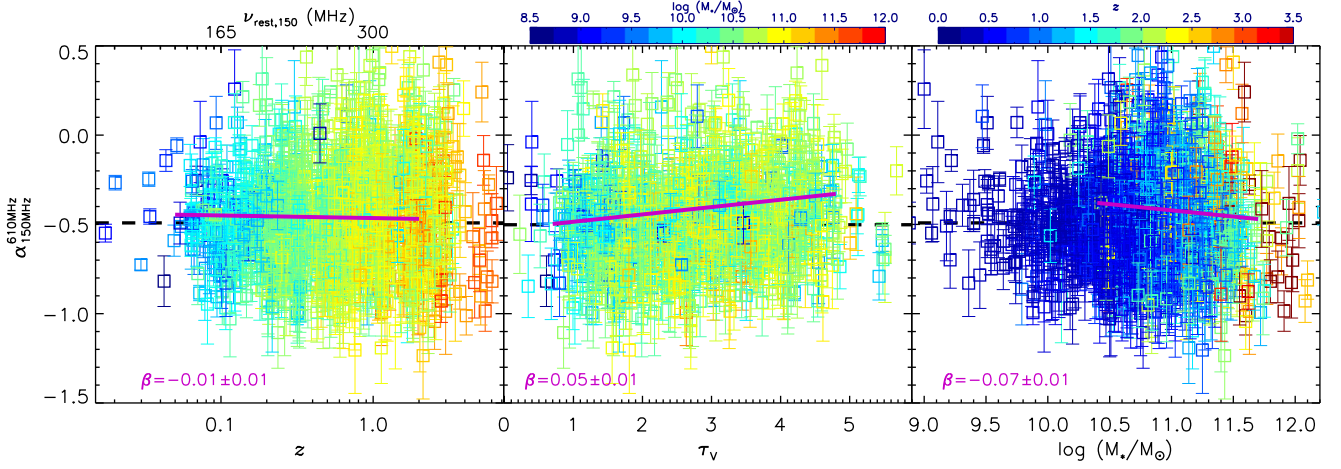


**Figure 7.** Radio spectral index between observer-frame frequencies of 150–610 MHz as functions of redshift (*left*), optical depth at V-band (*middle*), and stellar mass (*right*) for the SFGs detected from GMRT-wide (Ishwara-Chandra et al. 2020). The colour of symbols represents the redshift in the right panel and the stellar mass in the other two panels. To reduce the effect from the incompleteness of our radio flux-limited sample, we limit the SFGs to  $z < 2$  and  $\log(M_*/M_\odot) > 10.4$  when fitting the correlations between  $\alpha_{150}^{610}$  and redshift, and stellar mass respectively. On average, the radio spectral slope of SFGs at observed 150–610 MHz flattens with increasing optical depth and steepens with increasing stellar mass, although we do not find significant correlation between  $\alpha_{150}^{610}$  and redshift (rest-frame frequency).

#### 4.3.1 Radio spectral indices at observed 150–385 MHz and 385–610 MHz

We show the radio spectral index between observer-frame frequencies of 150–385 MHz as a function of the separation between LOFAR 150 MHz and uGMRT 400 MHz detections for these 1,194 SFGs in the left panel of Figure 8. According to the distribution of  $\alpha_{150}^{385}$ , we choose  $r_{150-385} = 2''.5$  as the cut when cross-matching the uGMRT 400 MHz and LOFAR 150 MHz sources. There are 20 SFGs with  $r_{150-385} < 2''.5$  that have  $\alpha_{150}^{385} - \sigma_{150}^{385} > 0.3$ , which means that they have very flat radio spectra at observed 150–385 MHz. Our visual inspection shows that three of them are resolved as two components at LOFAR 150 MHz. There are also two SFGs with  $\alpha_{150}^{385} + \sigma_{150}^{385} < -0.8$ , i.e., with very steep radio spectra at observed 150–385 MHz. We find that both of them are resolved at LOFAR 150 MHz. We therefore remove these five sources from our sample and show the distribution of  $\alpha_{150}^{385}$  for the remaining 1,158 SFGs with  $r_{150-385} < 2''.5$  in Figure 8. The median radio spectral index between observer-frame frequencies of 150–385 MHz is  $\alpha_{150}^{385} = -0.29 \pm 0.01$  with a scatter of  $\sigma = 0.31$ .

For the 1,194 SFGs that have both uGMRT 400 MHz and LOFAR 150 MHz detections, 1,038 also have a GMRT 610 MHz counterpart within  $10''$ . We show their radio spectral indices between observer-frame frequencies of 150–610 MHz as a function of the separation between LOFAR 150 MHz and GMRT 610 MHz detections in the middle panel of Figure 8. Among them, 896 have  $r_{150-610\text{MHz}} < 2''.0$  after we remove the sources that are resolved at LOFAR 150 MHz. The median  $\alpha_{150}^{610}$  for these 896 uGMRT 400 MHz-selected SFGs is  $\alpha_{150}^{610} = -0.52 \pm 0.01$  with a scatter of  $\sigma = 0.23$ , which is consistent with the results based on GMRT 610 MHz-detected SFGs (Section §4.1 and §4.2).

We also show the radio spectral index between observer-frame frequencies of 385–610 MHz as a function of the separation between uGMRT 400 MHz and GMRT 610 MHz detections for the 1,038 uGMRT 400 MHz-selected SFGs that have a GMRT 610 MHz counterpart within  $10''$  in the right panel of Figure 8. According to the distribution of  $\alpha_{385}^{610}$ , we choose  $r_{385-610} = 2''.5$  as the cut when cross-matching uGMRT 400 MHz and GMRT 610 MHz sources. There are

926 uGMRT 400 MHz-selected SFGs that have  $r_{385-610} < 2''.5$  after we remove the SFGs that are resolved at LOFAR 150 MHz. The median spectral index is  $\alpha_{385}^{610} = -0.91^{+0.02}_{-0.03}$  with a scatter of  $\sigma = 0.66$ . The differences in spectral slope above and below 385 MHz occur because of the relatively shallower uGMRT 400 MHz data, i.e., the radio spectral indices we measured are flatter over the 150–385 MHz and steeper over the 385–610 MHz (Eddington bias).

To get a less biased sample in studying radio spectrum at observer-frame frequencies of 150–385 MHz and 385–610 MHz, we instead select the sample for study by applying a flux density cut at GMRT 610 MHz. The coverages of GMRT deep 610 MHz and uGMRT 400 MHz are slightly offset as shown in Figure 1. Within the overlapped region, only 47% (2,024/4,269) of GMRT 610 MHz sources have a 400 MHz counterpart within  $10''$ . We therefore limit the sources to  $S_{610\text{MHz}} > 300 \mu\text{Jy}$  to guarantee that  $>80\%$  of GMRT 610 MHz sources have a 400 MHz counterpart. Within the overlapped region, there are 303 SFGs with  $S_{610\text{MHz}} > 300 \mu\text{Jy}$ . Among them, 258 have a 400 MHz counterpart within  $2''.5$ . All of them also have a LOFAR 150 MHz counterpart within  $2''.0$  thanks to the high sensitivity of LOFAR data. The median spectral index between observer-frame frequency of 150–385 MHz, 385–610 MHz, and 150–610 MHz are  $\alpha_{150}^{385} = -0.42^{+0.03}_{-0.02}$ ,  $\alpha_{385}^{610} = -0.44^{+0.03}_{-0.04}$ , and  $\alpha_{150}^{610} = -0.42^{+0.02}_{-0.01}$ , which are consistent with the results from nearby brighter galaxies (Marvil et al. 2015).

#### 4.3.2 Radio spectral properties at 150–385 MHz and 385–610 MHz

For SFGs with  $S_{610\text{MHz}} > 300 \mu\text{Jy}$  and with detections at GMRT 610 MHz, uGMRT 400 MHz, and LOFAR 150 MHz, we show the correlations between their radio spectral indices and redshift, optical depth at V-band, and stellar mass in Figure 9. We find that, on average, the radio spectra at observer-frame frequency of 150–385 MHz and 385–610 MHz are not significantly correlated with redshift, i.e., rest-frame frequency, but flatten with increasing optical depth and steepen with increasing stellar mass. Consequently, the difference between radio spectral indices at observer-frame frequency of 150–385 MHz

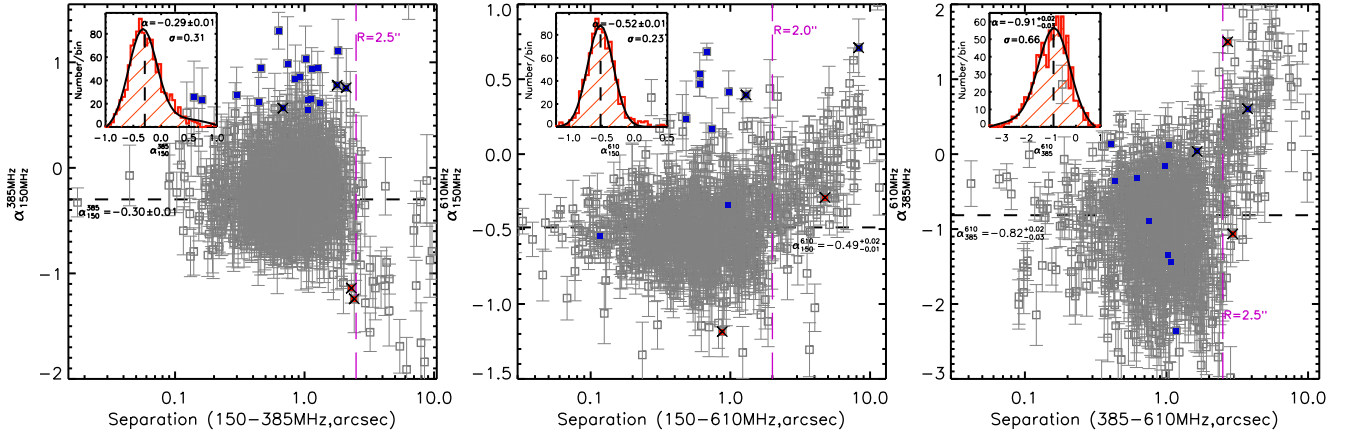


**Figure 8.** Radio spectral index between the observer-frame frequencies of 150–385 MHz (*left*), 150–610 MHz (*middle*), and 385–610 MHz (*right*) plotted against the separation between each pair of frequencies for the uGMRT 400 MHz-detected radio sources. *Left:* The purple dashed line marks the cross-match radius of  $r_{150-385} = 2''.5$ , which is chosen by the distribution of  $\alpha_{150}^{385}$  for the 1,194 uGMRT 400 MHz SFGs that have a LOFAR 150 MHz counterparts within  $10''$ . The blue squares are the 20 SFGs with  $r_{150-385} < 2''.5$  and  $\alpha_{150}^{385} - \sigma > 0.3$ , while the red squares are the two SFG with  $\alpha_{150}^{385} + \sigma < -0.8$ . Our visual inspection shows that five of them are resolved at LOFAR 150 MHz, which are marked by black crosses. We remove these five sources and show the distribution of  $\alpha_{150}^{385}$  for the remaining 1,158 SFGs with  $r_{150-385} < 2''.5$  in the left-top inset plot. The red dashed line marks their median spectral index of  $\alpha_{150}^{385} = -0.29 \pm 0.01$  with a scatter of  $\sigma = 0.31$ . *Middle:* For these 1,194 uGMRT 400 MHz SFGs, 1,038 also have a GMRT 610 MHz counterpart within  $10''$ . After removing the sources that are resolved at LOFAR 150 MHz, we obtain a sample of 896 SFGs with  $r_{150-610} < 2''.0$  and a median spectral index of  $\alpha_{150}^{610} = -0.52 \pm 0.01$  with a scatter of 0.23 as shown in the left-top inset plot. *Right:* We also apply a cross-match radius of  $r_{385-610} = 2''.5$  (purple dashed line) and obtain a sample of 926 SFGs that have detections at both uGMRT 400 MHz and GMRT 610 MHz. The median spectral index of these SFGs is  $\alpha_{385}^{610} = -0.91^{+0.02}_{-0.03}$  with a scatter of  $\sigma = 0.66$  as shown in the left-top inset plot.

and 385–610 MHz, i.e., spectral curvature, is not correlated with these physical properties as shown in the third row of Figure 9.

#### 4.4 JVLA 5 GHz as the selection frequency

Although the JVLA 5 GHz observations only cover the central  $0.13 \text{ deg}^2$  of the ELAIS-N1 field, the sensitivity reaches  $\sim 1 \mu\text{Jy beam}^{-1}$ . We therefore use JVLA 5 GHz as the selection frequency to study the radio spectral properties for radio-selected SFGs at observer-frame frequencies of 150–5000 MHz.

##### 4.4.1 Radio spectral indices at observed 150–5000 MHz

Because of a relatively higher angular resolution of JVLA 5 GHz data, we use a radius of  $3''.0$  when cross-matching the JVLA 5 GHz sources with the radio sources detected at 610 MHz, 400 MHz, or 150 MHz. We find that applying a smaller matching radius, i.e.,  $1''.5$ , does not change the median radio spectral indices at observer-frame frequencies of 385–5000 MHz and 150–5000 MHz, and only makes the median radio spectrum at 610–5000 MHz slighter flatter. We therefore keep all the 610 MHz, 400 MHz, and 150 MHz sources that are matched with the JVLA 5 GHz within  $3''.0$  in the following analyses.

For the 387 JVLA 5 GHz-detected sources in Taylor et al. (2014), 210 of them are cross-matched with a GMRT 610 MHz sources within  $3''.0$ . Among them, 137 are classified as SFGs in Ocran et al. (2020). We also remove 72 JVLA 5 GHz sources that have a LOFAR counterparts and are classified as AGN by Best et al. submitted. The overlap of the two AGN samples is 35. For the remaining 100 SFGs, we show the measured radio spectral index at observer-frame frequency of 610–5000 MHz,  $\alpha_{610}^{5000}$ , as a function of the separation between JVLA 5 GHz and GMRT 610 MHz detections in Figure 10. The median is  $\alpha_{610}^{5000} = -1.14^{+0.03}_{-0.05}$  with a scatter of  $\sigma = 0.32$ .

There are 168 of the 387 JVLA 5 GHz sources that have an uGMRT

400 MHz counterpart within  $3''.0$ . By removing the 31 and 65 AGN classified in Ocran et al. (2020) and Best et al. submitted respectively, we obtain a median radio spectral index of  $\alpha_{385}^{5000} = -1.08^{+0.01}_{-0.02}$  for a sample of 81 SFGs (Figure 10). The standard deviation of the measured radio spectral indices for these SFGs is  $\sigma = 0.21$ .

There are 217 JVLA 5 GHz sources that are matched with a LOFAR 150 MHz source within  $3''.0$ . Among them 133 are classified as SFGs in Best et al. submitted. We also remove additional five AGN that are classified in Ocran et al. (2020). For the remaining 128 SFGs in our sample, the median radio spectral index at observer-frame frequency of 150–5000 MHz is  $\alpha_{150}^{5000} = -0.87^{+0.01}_{-0.02}$  with a scatter of  $\sigma = 0.18$ .

##### 4.4.2 Radio spectral properties at observed 150–5000 MHz

We show the measured radio spectral indices at observer-frame frequencies of 610–5000 MHz, 385–5000 MHz and 150–5000 MHz as functions of redshift, optical depth at V-band, and stellar mass in Figure 11. We find that, on average, the radio spectrum of SFGs slightly steepens with increasing redshift and stellar mass at 150–5000 MHz. However, there is no significant correlation between radio spectral index and optical depth at V-band, which is different from that at low-frequency ( $\nu < 1 \text{ GHz}$ , Figure 5 and Figure 9).

For the 100 SFGs that have both JVLA 5 GHz and GMRT 610 MHz (deep) detections, 82 of them also have a LOFAR 150 MHz counterpart within  $2''.0$  (the cross matching radius between GMRT 610 MHz and LOFAR 150 MHz sources). Although the sample size is very limited and the JVLA 5 GHz data is deeper than the data at the other two frequencies, we find that the difference between radio spectral indices at observer-frame frequencies of 150–610 MHz and 610–5000 MHz is not correlated with redshift (rest-frame frequency) and stellar mass but positively correlated with optical depth at V-band weakly. This is not surprising given the lack of significant correlation between the

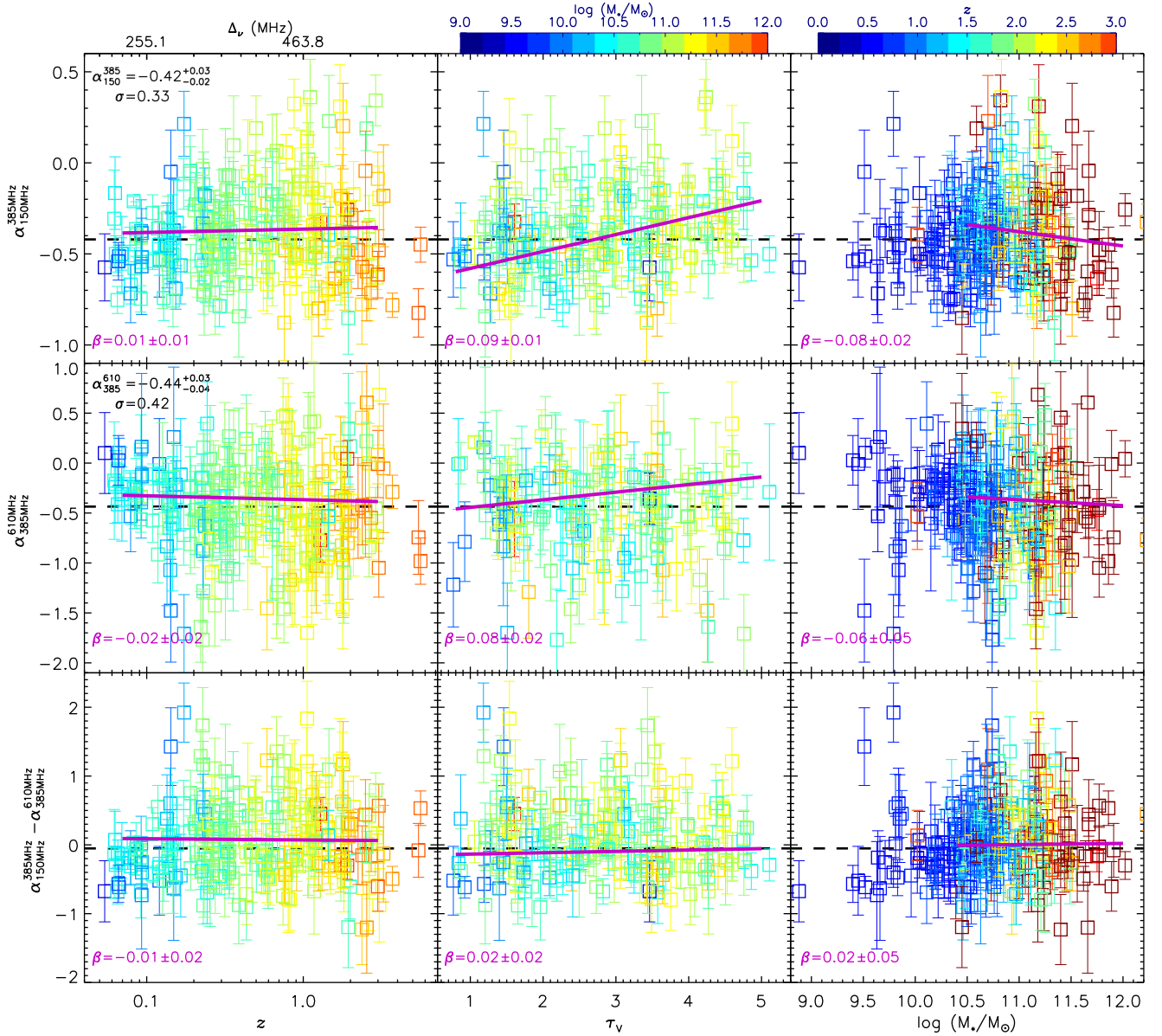


**Figure 9.** Radio spectral indices at observer-frame frequencies of 150–385 MHz (first row), 385–610 MHz (second row), and the difference between them (third row) as functions of redshift (left column), optical depth at V-band (middle column), and stellar mass (right column) for the 258 SFGs that have  $S_{610\text{MHz}} > 300 \mu\text{Jy}$  and detections at both uGMRT 400 MHz and LOFAR 150 MHz. As shown in the first column, the radio spectral indices at both 150–385 MHz and 385–610 MHz are not significantly correlated with redshift, i.e., rest-frame frequency. The second and third columns show that, on average, the radio spectra at both frequency ranges slightly flatten with optical depth and steepen with stellar mass. However, the difference between  $\alpha_{150}^{385}$  and  $\alpha_{385}^{610}$  (spectral curvature) does not have significant correlations with these physical properties.

radio spectral index and the V-band optical depth at  $\nu > 1$  GHz as shown in Figure 11.

## 5 DISCUSSION

By combining the LOFAR 150 MHz, uGMRT 400 MHz, GMRT 610 MHz, and JVLA 5 GHz data in the ELAIS-N1 field, we study the radio spectral properties at observer-frame frequencies of 150–5000 MHz. Here we discuss the possible physical mechanisms that determine the radio spectrum at this frequency range.

### 5.1 Radio spectral indices at observer-frame 150–5000 MHz

By using the two radio datasets with the greatest sensitivity and coverage in this work, we obtain a total of  $\sim 3,500$  SFGs that have detections at both GMRT 610 MHz and LOFAR 150 MHz and a median spectral index of  $\alpha_{610}^{150} = -0.51 \pm 0.01$ . Our measurement is consistent with the median spectral indices at similar frequency ranges of nearby galaxies (Marvil et al. 2015; Chyży et al. 2018) and submillimeter-selected galaxies (SMGs, Ramasawmy et al. 2021). We note that Chyży et al. (2018) and Ramasawmy et al. (2021) also include the  $\sim 150$  MHz data in their analyses from the LOFAR Multifrequency Snapshot Sky Survey and the LoTSS respectively. However, compared with the median radio spectral index at high fre-



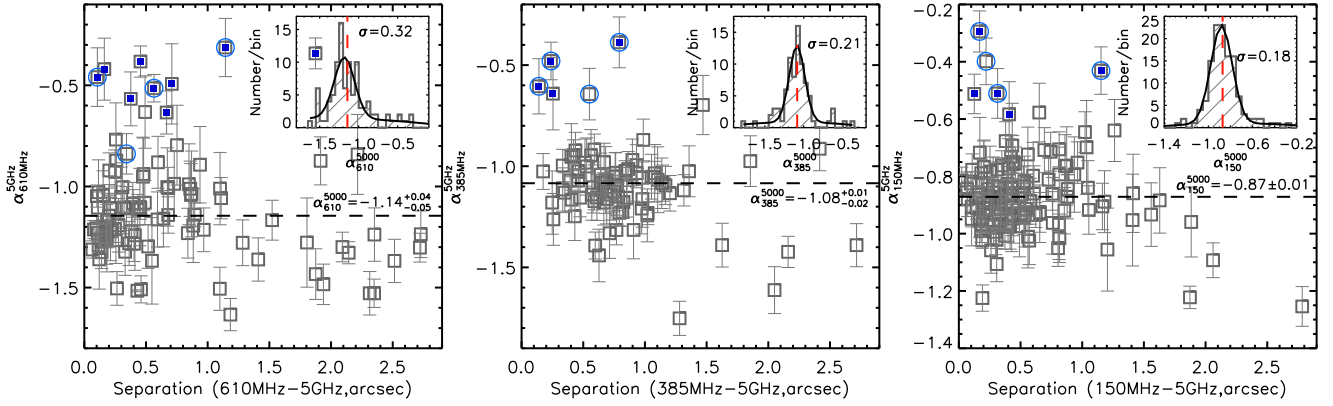


**Figure 10.** Radio spectral index between the observer-frame frequencies of 610–5000 MHz (*left*), 385–5000 MHz (*middle*) and 150–5000 MHz (*right*) plotted against the separation between the respective frequencies for JVLA 5 GHz detected SFGs. The black dashed lines represent the median spectral indices of  $\alpha_{610}^{5000} = -1.14^{+0.04}_{-0.05}$ ,  $\alpha_{385}^{5000} = -1.08^{+0.01}_{-0.02}$ , and  $\alpha_{150}^{5000} = -0.87 \pm 0.01$  for samples of 100, 81, and 128 SFGs that have detections at each pair of frequencies respectively. We show the distribution of these measured radio spectral indices and their standard deviation in the left-top inset plot of each panel. The blue squares are the nine SFGs with  $\alpha_{610}^{5000} - \alpha_{610}^{5000} > -0.8$ . The four blue circles mark the SFGs with  $\alpha_{385}^{5000} - \alpha_{385}^{5000} > -0.8$ . We find that their radio spectra are also flatter at observer-frame frequencies of 150–5000 MHz. Our visual inspection suggests that none of them is resolved at JVLA 5 GHz.

quency, specifically, at rest-frame  $\sim 1.3$ –10 GHz in [An et al. \(2021\)](#), as well as the synchrotron spectrum, the radio spectrum of SFGs is flatter at  $\nu_{\text{rest}} < \sim 1$  GHz.

JVLA 5 GHz data have an RMS noise of  $1.05 \mu\text{Jy}$ , which corresponds to  $\sim 6 \mu\text{Jy}$ ,  $\sim 8 \mu\text{Jy}$ , and  $\sim 17 \mu\text{Jy}$  at 610 MHz, 385 MHz, and 150 MHz respectively if we assume a radio spectral index of  $\alpha = -0.8$  (synchrotron spectrum). Therefore, using 5 GHz as the selection frequency biases the sample to SFGs with a relatively steeper radio spectrum, which causes the median radio spectral slope at observer-frame frequencies of 610–5000 MHz, 385–5000 MHz and 150–5000 MHz to be steeper than that of the synchrotron spectrum as shown in Section 4.4.1.

Although including the JVLA 5 GHz data biases the sample to SFGs with a relatively steeper radio spectrum because of the high-sensitivity of the data, the radio spectrum is flatter if we include a lower frequency dataset when measuring the radio spectral index between observer-frame frequency of 150–5000 MHz as shown in Figure 10. However, the high-sensitivity of LOFAR 150 MHz data is also the reason for a flatter radio spectrum at 150–5000 MHz. Based on the correlations between radio spectral indices and physical properties of SFGs we find in this work, we will discuss the possible physical mechanisms that cause the radio spectrum to be flatter at low frequency ( $\nu_{\text{rest}} < \sim 1$  GHz) than at high frequency in Section 5.2.

## 5.2 Radio spectral properties at observer-frame 150–5000 MHz

For radio-selected SFGs, we find that, on average, their radio spectrum slightly steepens with increasing stellar mass at any frequency ranges analysed in this work. However, we only find that at  $\nu_{\text{obs}} < \sim 1$  GHz, the radio spectrum of SFGs slightly flattens with increasing optical depth. This results a positive correlation between spectral curvature ( $\alpha_{150}^{610} - \alpha_{610}^{5000}$ ) and optical depth at V-band. At  $\nu_{\text{obs}} < \sim 1$  GHz, the difference between radio spectra indices ( $\alpha_{150}^{385} - \alpha_{385}^{610}$ ) is not significantly correlated with physical properties of SFGs. This phenomenon has been reported in [Calistro Rivera et al. \(2017\)](#), which found that the spectral curvature at observer-frequency of 150–1400 MHz does not dependent on redshift, SFR, and specific SFR of SFGs. In addition, the median radio spectral indices we measured at 150–5000 MHz indicate that the radio spectrum is flatter at

low frequency than at high frequency. Here we discuss the possible explanations of these correlations.

### 5.2.1 Radio spectrum steepens with increasing stellar mass

At observer-frame frequency of 150–5000 MHz, we find that the radio spectrum slightly steepens with increasing stellar mass. This correlation has been reported in our previous work that studied radio spectral properties at observer-frame frequency of 1.3–3 GHz by combining the MeerKAT 1.3 GHz and VLA 3 GHz data in the COSMOS field ([An et al. 2021](#)). In that work, we noted that this correlation could be explained by age-related synchrotron loss. For the relativistic CR electron, the critical frequency, at which the electron emits most of its energy, is proportional to the square of its energy and the strength of the perpendicular component of the magnetic field, i.e.,

$$\nu_c \propto E^2 B_{\perp}. \quad (1)$$

If we only take synchrotron radiation in account, the lifetime of a CR electron is

$$t_{\text{sy}} \propto \nu_c^{-0.5} B_{\perp}^{-1.5}. \quad (2)$$

Therefore, high-energy CR electrons lose their energy faster than that of low-energy CR electrons. Similarly, the inverse Compton loss of these CR electrons is also greater at high frequency ([Pacholczyk 1970](#)). For SFGs, fresh CR electrons are constantly injected in the star-forming regions, which keeps the radio spectral slope constant. We therefore discussed in [An et al. \(2021\)](#) that the slightly increased ratio of aged and young relativistic CR electrons with increasing stellar mass, could be a physical cause leading to radio spectrum steepening for massive SFGs.

### 5.2.2 Radio spectrum flattens with increasing optical depth at $\nu < \sim 1$ GHz

At  $\nu_{\text{obs}} < \sim 1$  GHz, the radio spectrum of SFGs slightly flattens with increasing optical depth at V-band. However, this correlation is not found when we include the high-frequency JVLA 5 GHz data, although the sample size of 5 GHz-detected sources is very limited because of the small coverage of the data.

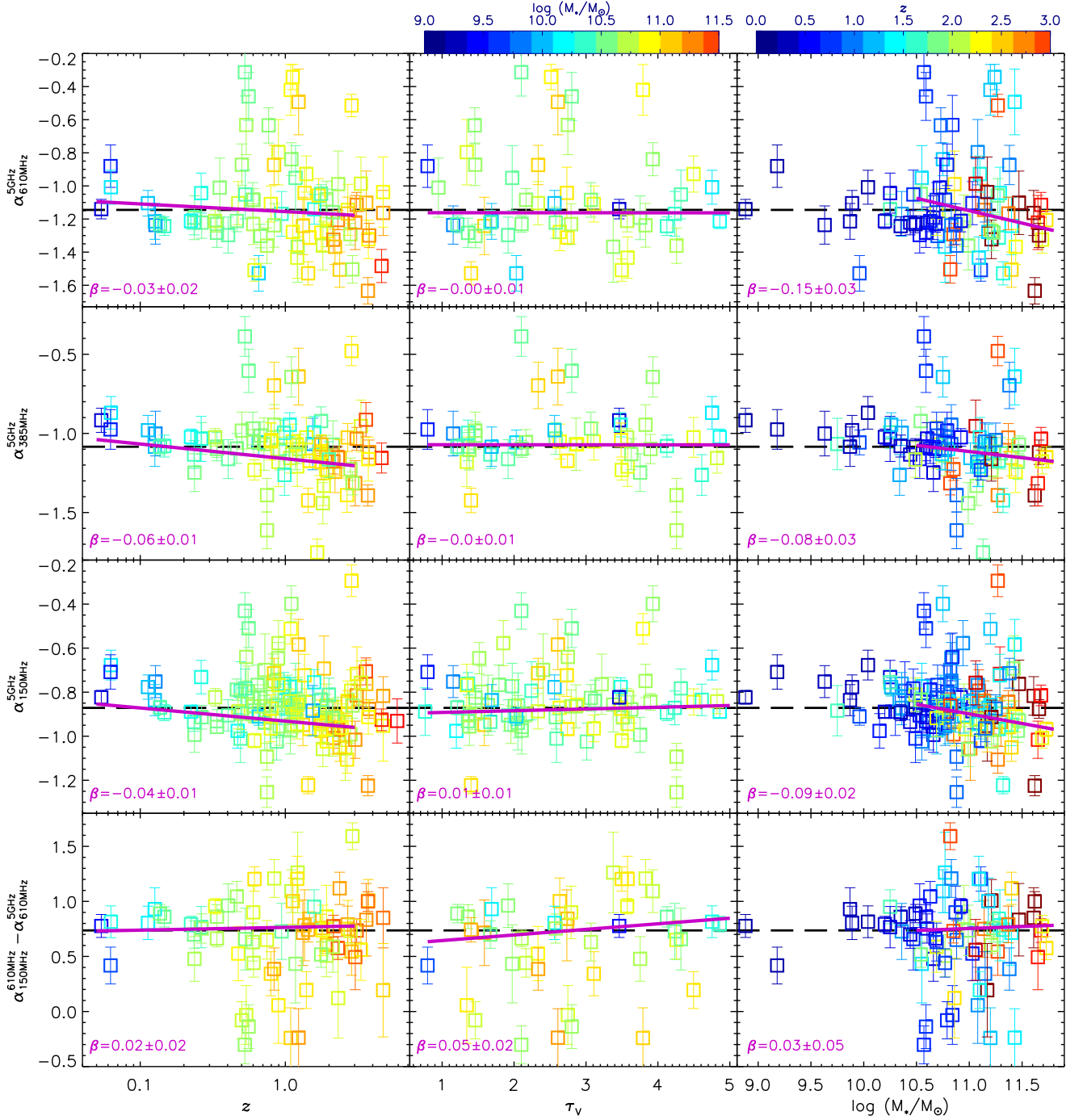


**Figure 11.** Radio spectral indices at observer-frame 610–5000 MHz (*first row*), 400–5000 MHz (*second row*), 150–5000 MHz (*third row*), and  $(\alpha_{150}^{610} - \alpha_{610}^{5000})$  as functions of redshift (rest-frame frequency), optical depth at V-band, and stellar mass of SFGs respectively. The plots in the first column show that the radio spectrum of SFGs flattens at low-frequency. The second column shows that the radio spectra at these frequency ranges do not have significant correlations with optical depth at V-band, in contrast to the radio spectrum at  $\nu_{\text{obs}} < \sim 1$  GHz (Figure 5 and 9). However, similar to the trend at  $\nu_{\text{obs}} < \sim 1$  GHz, the radio spectrum steepens with increasing stellar mass as shown by the plots in the last column. The plots in the last row show that the difference between radio spectra indices at observer-frame 150–610 MHz and 610–5000 MHz is not correlated with redshift and stellar mass but positively correlated with optical depth at V-band weakly.

The effective optical depth at V-band depends on the relative distribution of the diffuse gas and dust along the line of sight. SFGs with higher optical depth at V-band are expected to have higher column density of free electron ( $n_e$ ) along the line of sight. Besides, these electrons might be more associated with colder regions around the star formation sites in SFGs. Therefore they are affected more

by free-free absorption because the absorption coefficient has the following form (Condon 1992):

$$\kappa \propto n_e^2 T_e^{-1.35} \nu^{-2.1}, \quad (3)$$

where  $T_e$  is the electron temperature of the HII emitting region. This equation and other theoretical models as well as previous observa-

tions show that the effect of thermal free-free absorption increases at low frequency (Condon 1992; McDonald et al. 2002; Tingay 2004; Murphy 2009; Clemens et al. 2010; Lacki 2013; Kapińska et al. 2017; Galvin et al. 2018; Klein et al. 2018; Dey et al. 2022), which explains why we only find the correlation between optical depth at V-band and radio spectrum at low frequency.

### 5.2.3 The low-frequency radio spectrum is flatter than the high-frequency

As discussed in Section §5.1, our measured median radio spectral index at observer-frame frequency of 150–50000 MHz show that, on average, the radio spectrum of SFGs is flatter at low frequency than at high frequency. However, when we investigate the measured radio spectral index as a function of rest-frame frequency (redshift) at either frequency range, i.e., 150–610 MHz (Figure 5) or 385–610 MHz (Figure 9), we only find a very weak or even negligible correlation because of the large scatter of measured radio spectral indices at any given rest-frame frequencies.

The correlations of SFGs' radio spectral slope with the stellar mass and with the optical depth at V-band suggest that both spectral ageing of CR electrons and thermal free-free absorption could be the physical causes of why the radio spectrum is flatter at low frequency than at high frequency. These two physical mechanisms are also used as the main explanations for the different radio spectral slopes at low and high frequency in the literature (e.g., Condon 1992; McDonald et al. 2002; Murphy 2009; Clemens et al. 2010; Lacki 2013; Marvil et al. 2015; Kapińska et al. 2017; Chyży et al. 2018; Galvin et al. 2018; Klein et al. 2018; Dey et al. 2022). The other mechanisms, such as synchrotron self-absorption and the Razin-Tsytovich effect, may also flatten the radio spectrum at low-frequency. However, synchrotron self-absorption requires extremely high brightness temperatures in order to be significant, and so its impact in SFGs is expected to be weak (e.g., Tingay 2004; Clemens et al. 2010). The Razin-Tsytovich effect can suppress synchrotron emission below the Razin frequency,

$$\nu_R \propto n_e B^{-1}. \quad (4)$$

This effect may dominate over internal free-free absorption when the thermal gas is considerably hotter than  $10^4$  K, which is rarely attained by normal SFGs (e.g., Condon et al. 1991; Lacki 2013; Chyży et al. 2018).

As shown by Equation 1 to 4, the magnetic field ( $B$ ), column density of free electrons ( $n_e$ ), and electron temperature ( $T_e$ ) in the HII region are the key features of the physical mechanisms that are responsible for the different radio spectral slopes at low and high frequency discussed above. Studies of radio spectrum of nearby galaxies and theoretical simulations of CR electron propagation discussed the effect of these individual physical parameters as well as some other physical conditions, such as galactic wind (e.g., Heesen et al. 2016; Mulcahy et al. 2018; Winner et al. 2019; Werhahn et al. 2021; Stein et al. 2022).

In contrast, one advantage of our statistical studies is the ability to suggest possible causes of why the radio spectrum is flatter at low frequency than at high frequency. In particular, we find that the correlations between the SFGs' integrated radio spectrum and their astrophysical properties could lend support to spectral ageing and thermal free-free absorption as two possible main mechanisms for our samples.

## 6 CONCLUSION

By combining high-sensitivity LOFAR 150 MHz, uGMRT 400 MHz, GMRT 610 MHz, and JVLA 5 GHz data in the ELAIS-N1 field, we measure the radio spectral indices between observer-frame frequency of 150–5000 MHz and study their correlations with physical properties of SFGs. The main conclusions from our work are as follows.

1) We obtain  $\sim 3,500$  SFGs that have detections at both GMRT 610 MHz and LOFAR 150 MHz by removing AGN from the two radio samples. The median radio spectral index for these SFGs is  $\alpha_{150}^{610} = -0.51 \pm 0.01$  with a scatter of  $\sigma = 0.2$ . Therefore, the radio spectrum at 150–610 MHz is flatter than that at high frequency ( $\nu_{\text{rest}} > \sim 1$  GHz) and the synchrotron spectrum.

2) Because of the relatively low-sensitivity of uGMRT 400 MHz data, we limit our sample to the SFGs with  $S_{610\text{MHz}} > 300 \mu\text{Jy}$ , and obtain a median spectral indices of  $\alpha_{150}^{385} = -0.42^{+0.03}_{-0.02}$ ,  $\alpha_{385}^{610} = -0.44^{+0.03}_{-0.04}$  and  $\alpha_{150}^{610} = -0.42^{+0.02}_{-0.01}$ .

3) Although JVLA 5 GHz data has very limited coverage, and its high-sensitivity biases the sample to SFGs with a relatively steeper radio spectrum, we obtain median  $\alpha_{610}^{5000} = -1.14^{+0.04}_{-0.05}$ ,  $\alpha_{385}^{5000} = -1.08^{+0.01}_{-0.02}$  and  $\alpha_{150}^{5000} = -0.87 \pm 0.01$  for samples of  $\sim 100$  SFGs that have detections at the two corresponding frequencies. Therefore, we find that the radio spectrum is flatter if we include a lower frequency dataset, although the high sensitivity of LOFAR 150 MHz data is also the reason for a flatter radio spectrum at 150–5000 MHz.

4) We correlate the measured radio spectral indices with physical properties of SFGs and find that, on average, the radio spectrum steepens with increasing stellar mass at observer-frame frequency of 150–5000 MHz. We discuss that the spectral ageing due to the energy loss of relativistic CR electrons via synchrotron and inverse Compton radiation could explain this trend.

5) At  $\nu_{\text{obs}} < \sim 1$  GHz, we find that, on average, the radio spectrum slightly flattens with increasing optical depth at V-band of radio-selected SFGs. However, this correlation is not found when we include the high-frequency JVLA 5 GHz data. We suggest that thermal free-free absorption is a possible underlying physical mechanism of this correlation.

6) Our statistical study of the correlation between integrated radio spectrum and physical properties of SFGs suggests the spectral ageing of CR electrons and thermal free-free absorption as two main physical mechanisms that cause the radio spectrum to be flatter at low frequency than at high frequency.

FXA and MV acknowledge financial support from the Inter-University Institute for Data Intensive Astronomy (IDIA), a partnership of the University of Cape Town, the University of Pretoria, the University of the Western Cape, and the South African Radio Astronomy Observatory. FXA is grateful for support from the National Science Foundation of China (12233005, 12073078, and 12173088). MV acknowledges the support from the South African Department of Science and Innovation's National Research Foundation under the ISARP RADIOSKY2020 Joint Research Scheme (DSI-NRF Grant Number 113121) and the CSUR HIPPO Project (DSI-NRF Grant Number 121291). PNB and RK acknowledge support from the UK STFC via grant ST/V000594/1.

We acknowledge the use of the ilifu cloud computing facility –www.ilifu.ac.za, a partnership of the University of Cape Town (UCT), the University of the Western Cape, the University of Stellenbosch, Sol Plaatje University, the Cape Peninsula University of Technology, and the South African Radio Astronomy Observatory. The ilifu facility is supported by contributions from the IDIA, the Computational Biology division at UCT, and the Data Intensive Research Initiative of South Africa (DIRISA).



## DATA AVAILABILITY

The LOFAR 150 MHz data used for the analysis of this paper are publicly available at <https://lofar-surveys.org/deepfields.html>. The GMRT 610 MHz and JVLA 5 GHz data used in this research will be shared upon reasonable request to the corresponding author.

## REFERENCES

- Aihara H., et al., 2018, *PASJ*, **70**, S8
- Algera H. S. B., et al., 2021, *ApJ*, **912**, 73
- Algera H. S. B., et al., 2022, *ApJ*, **924**, 76
- An F., et al., 2021, *MNRAS*, **507**, 2643
- Bell E. F., 2003, *ApJ*, **586**, 794
- Bolton A. S., et al., 2012, *AJ*, **144**, 144
- Bonato M., et al., 2021, *A&A*, **656**, A48
- Bonzini M., Padovani P., Mainieri V., Kellermann K. I., Miller N., Rosati P., Tozzi P., Vattakunnel S., 2013, *MNRAS*, **436**, 3759
- Bressan A., Silva L., Granato G. L., 2002, *A&A*, **392**, 377
- Calistro Rivera G., Lusso E., Hennawi J. F., Hogg D. W., 2016, *ApJ*, **833**, 98
- Calistro Rivera G., et al., 2017, *MNRAS*, **469**, 3468
- Carnall A. C., McLure R. J., Dunlop J. S., Davé R., 2018, *MNRAS*, **480**, 4379
- Chabrier G., 2003, *PASP*, **115**, 763
- Chakraborty A., et al., 2019, *MNRAS*, **490**, 243
- Chambers K. C., et al., 2016, arXiv e-prints, p. arXiv:1612.05560
- Charlot S., Fall S. M., 2000, *ApJ*, **539**, 718
- Chyży K. T., et al., 2018, *A&A*, **619**, A36
- Clemens M. S., Scaife A., Vega O., Bressan A., 2010, *MNRAS*, **405**, 887
- Condon J. J., 1992, *ARA&A*, **30**, 575
- Condon J. J., Huang Z. P., Yin Q. F., Thuan T. X., 1991, *ApJ*, **378**, 65
- Delhaize J., et al., 2017, *A&A*, **602**, A4
- Delvecchio I., et al., 2021, *A&A*, **647**, A123
- Dey S., Goyal A., Małek K., Galvin T. J., Seymour N., Santos T. D., Piotrowska J., Charmandaris V., 2022, *ApJ*, **938**, 152
- Donley J. L., et al., 2012, *ApJ*, **748**, 142
- Duncan K. J., et al., 2021, *A&A*, **648**, A4
- Fleishman G. D., Tokarev Y. V., 1995, *A&A*, **293**, 565
- Galvin T. J., Seymour N., Filipović M. D., Tothill N. F. H., Marvil J., Drouart G., Symeonidis M., Huynh M. T., 2016, *MNRAS*, **461**, 825
- Galvin T. J., et al., 2018, *MNRAS*, **474**, 779
- Gim H. B., et al., 2019, *ApJ*, **875**, 80
- Heesen V., Dettmar R.-J., Krause M., Beck R., Stein Y., 2016, *MNRAS*, **458**, 332
- Helou G., Soifer B. T., Rowan-Robinson M., 1985, *ApJ*, **298**, L7
- Hindson L., et al., 2018, *ApJS*, **234**, 29
- Ishwara-Chandra C. H., Taylor A. R., Green D. A., Stil J. M., Vaccari M., Ocran E. F., 2020, *MNRAS*, **497**, 5383
- Iverson R. J., et al., 2010, *A&A*, **518**, L31
- Kapińska A. D., et al., 2017, *ApJ*, **838**, 68
- Kennicutt R. C., Evans N. J., 2012, *ARA&A*, **50**, 531
- Klein U., Lisenfeld U., Verley S., 2018, *A&A*, **611**, A55
- Kondapally R., et al., 2021, *A&A*, **648**, A3
- Lacki B. C., 2010, *MNRAS*, **406**, 863
- Lacki B. C., 2013, *MNRAS*, **431**, 3003
- Lawrence A., et al., 2007, *MNRAS*, **379**, 1599
- Lonsdale C. J., et al., 2003, *PASP*, **115**, 897
- Lonsdale C. J., et al., 2009, *IEEE Proceedings*, **97**, 1497
- Magnelli B., et al., 2015, *A&A*, **573**, A45
- Mao M. Y., Huynh M. T., Norris R. P., Dickinson M., Frayer D., Helou G., Monkiewicz J. A., 2011, *ApJ*, **731**, 79
- Martin D. C., et al., 2005, *ApJ*, **619**, L1
- Marvil J., Owen F., Eilek J., 2015, *AJ*, **149**, 32
- Mauduit J. C., et al., 2012, *PASP*, **124**, 714
- McDonald A. R., Muxlow T. W. B., Wills K. A., Pedlar A., Beswick R. J., 2002, *MNRAS*, **334**, 912
- Morrissey P., et al., 2007, *ApJS*, **173**, 682
- Mulcahy D. D., et al., 2018, *A&A*, **615**, A98
- Murphy E. J., 2009, *ApJ*, **706**, 482
- Murphy E. J., et al., 2011, *ApJ*, **737**, 67
- Murphy E. J., et al., 2012, *ApJ*, **761**, 97
- Muzzin A., et al., 2009, *ApJ*, **698**, 1934
- Noll S., Burgarella D., Giovannoli E., Buat V., Marcellac D., Muñoz-Mateos J. C., 2009, *A&A*, **507**, 1793
- Ocran E. F., Taylor A. R., Vaccari M., Ishwara-Chandra C. H., Prandoni I., 2020, *MNRAS*, **491**, 1127
- Oke J. B., 1974, *ApJS*, **27**, 21
- Oliver S., et al., 2000, *MNRAS*, **316**, 749
- Oliver S. J., et al., 2012, *MNRAS*, **424**, 1614
- Pacholczyk A. G., 1970, Radio astrophysics. Nonthermal processes in galactic and extragalactic sources
- Pérez-Torres M., Mattila S., Alonso-Herrero A., Aalto S., Efstathiou A., 2021, *A&ARv*, **29**, 2
- Planck Collaboration et al., 2016, *A&A*, **594**, A13
- Ramasawmy J., et al., 2021, arXiv e-prints, p. arXiv:2103.09677
- Razin V., 1960, *Izvestiya Vysshikh Uchebnykh Zavedenii. Radiofizika*, **3**, 584
- Rieke G. H., et al., 2004, *ApJS*, **154**, 25
- Rowan-Robinson M., et al., 2004, *MNRAS*, **351**, 1290
- Roy S., 2013, *ApJ*, **773**, 67
- Sabater J., et al., 2021, *A&A*, **648**, A2
- Schleicher D. R. G., Beck R., 2013, *A&A*, **556**, A142
- Shimwell T. W., et al., 2017, *A&A*, **598**, A104
- Smith D. J. B., et al., 2021, *A&A*, **648**, A6
- Stein M., et al., 2022, arXiv e-prints, p. arXiv:2210.07709
- Swarup G., Ananthakrishnan S., Kapahi V. K., Rao A. P., Subrahmanya C. R., Kulkarni V. K., 1991, *Current Science*, **60**, 95
- Sweijen F., et al., 2022, *A&A*, **658**, A3
- Tasse C., et al., 2021, *A&A*, **648**, A1
- Taylor A. R., et al., 2014, in *Astronomical Society of India Conference Series*. pp 99–104 (arXiv:1405.0117), doi:10.48550/arXiv.1405.0117
- Thomson A. P., et al., 2019, *ApJ*, **883**, 204
- Tingay S. J., 2004, *AJ*, **127**, 10
- Vaccari M., 2015, in *The Many Facets of Extragalactic Radio Surveys: Towards New Scientific Challenges*. p. 27 (arXiv:1604.02353), doi:10.22323/1.267.0027
- Vaccari M., et al., 2005, *MNRAS*, **358**, 397
- Varenus E., et al., 2015, *A&A*, **574**, A114
- Voelk H. J., Klein U., Wielebinski R., 1989, *A&A*, **213**, L12
- Werhahn M., Pfrommer C., Girichidis P., 2021, *MNRAS*, **508**, 4072
- Whittam I. H., et al., 2022, *MNRAS*, **516**, 245
- Wills K. A., Pedlar A., Muxlow T. W. B., Wilkinson P. N., 1997, *MNRAS*, **291**, 517
- Wilson G., et al., 2009, *ApJ*, **698**, 1943
- Winner G., Pfrommer C., Girichidis P., Pakmor R., 2019, *MNRAS*, **488**, 2235
- Yun M. S., Reddy N. A., Condon J. J., 2001, *ApJ*, **554**, 803
- da Cunha E., Charlot S., Elbaz D., 2008, *MNRAS*, **388**, 1595
- van Haarlem M. P., et al., 2013, *A&A*, **556**, A2

This paper has been typeset from a  $\text{\LaTeX}$  file prepared by the author.